WestVirginiaUniversity
THE RESEARCH REPOSITORY @ WVU

Graduate Theses, Dissertations, and Problem Reports

2023

Drift Orbit Bifurcation Effects on Earth's Radiation Belt Electrons

Jinbei Huang
West Virginia University, jh0049@mix.wvu.edu

Follow this and additional works at: https://researchrepository.wvu.edu/etd

 Part of the Geophysics and Seismology Commons, and the Plasma and Beam Physics Commons

Recommended Citation

Huang, Jinbei, "Drift Orbit Bifurcation Effects on Earth's Radiation Belt Electrons" (2023). *Graduate Theses, Dissertations, and Problem Reports*. 12107.
https://researchrepository.wvu.edu/etd/12107

This Dissertation is protected by copyright and/or related rights. It has been brought to you by the The Research Repository @ WVU with permission from the rights-holder(s). You are free to use this Dissertation in any way that is permitted by the copyright and related rights legislation that applies to your use. For other uses you must obtain permission from the rights-holder(s) directly, unless additional rights are indicated by a Creative Commons license in the record and/ or on the work itself. This Dissertation has been accepted for inclusion in WVU Graduate Theses, Dissertations, and Problem Reports collection by an authorized administrator of The Research Repository @ WVU. For more information, please contact researchrepository@mail.wvu.edu.

Drift Orbit Bifurcation Effects on Earth's Radiation Belt Electrons

Jinbei Huang

Dissertation submitted
to the Eberly College of Arts and Sciences
at West Virginia University

in partial fulfillment of the requirements for the degree of

Doctor of Philosophy in
Physics

Weichao Tu, Ph.D. Chair

Paul Cassak, Ph.D.

Piyush Mehta, Ph.D.

Earl Scime, Ph.D.

Department of Physics and Astronomy

Morgantown, West Virginia

2023

Keywords: space physics, plasma physics, space plasma, inner magnetosphere, radiation belt electrons, adiabatic invariants, drift orbit bifurcation, space craft data analysis

Copyright 2023 Jinbei Huang

ABSTRACT

Drift Orbit Bifurcation Effects on Earth's Radiation Belt Electrons

Jinbei Huang

Energetic charged particles trapped in the Earth's radiation belt form a hazardous space environment for artificial electronic systems and astronauts. The study of Earth's radiation belt is becoming increasingly important with the development of communication technology, which plays a significant role in modern society. Earth's radiation belt is highly dynamic, and the electron flux can drop by several orders of magnitude within a few hours which is called radiation belt dropout. The fast dropout of energetic electrons in the radiation belt, despite its significance, has not been thoroughly studied. One of the most compelling outstanding questions in Earth's radiation belt studies is: "What physical mechanisms cause these rapid and substantial drops of radiation belt electron flux?" Apart from well-studied processes like wave-particle interaction, which contribute to the loss of radiation belt electrons through the processes including magnetopause shadowing and atmospheric precipitation, the effects from an anomalous process called drift orbit bifurcation (DOB) have not yet been fully understood. DOB has been suggested to play a major role in the loss and transport of radiation belt electrons since it violates the particles' second adiabatic invariant and makes the third invariant undefined. In our first study of this dissertation, using guiding-center test particle simulations based on the Tsyganenko-1989c magnetic field model we show that DOB could affect a broad region of the outer radiation belt. It can penetrate inside the geosynchronous orbit at $Kp \geqslant 3$, where Kp is a geomagnetic index that quantifies the general disturbance level of Earth's magnetosphere. Moreover, DOB effects are more significant further away from Earth, at higher Kp, and for higher electron energies. Specifically, the short-term simulation results after one electron drift show both traditional and nontraditional DOB transport of electrons, with the nontraditional DOB, caused by a third minimum of the magnetic field strength near the equator, reported by us for the first time. Moreover, our results show large ballistic jumps in the second invariant and radial distance for electrons at high equatorial pitch angles after one drift. In addition, long-term DOB transport coefficients of electrons over many drifts are calculated based on our simulation results. We find that the pitch angle and radial diffusion coefficients of electrons due to DOB could be comparable to or even larger than those caused by electron interactions with chorus and Ultra-Low-Frequency waves, respectively. Meanwhile, the last closed drift shell (LCDS) has been identified as a crucial parameter for investigating the magnetopause shadowing loss of radiation belt electrons. However, the DOB effects have not been physically incorporated into the LCDS calculation. In the second study of this dissertation, we calculate the event-specific LCDS using different approaches to dealing with the DOB effects, i.e., tracing field lines ignoring DOB, tracing test particles rejecting DOB, and tracing test particles including DOB, and then incorporate them into a radial diffusion model to simulate the fast electron dropout observed by Van Allen Probes in May 2017. The model effectively captures the fast dropout at high L^* (the third adiabatic invariant) and exhibits the best agreement with data when LCDS is calculated by tracing test particles and including DOB effects more realistically. This study represents the first quantitative modeling of the DOB effects on the radiation belt magnetopause shadowing loss via a more physical specification of LCDS. In summary, our results demonstrate that DOB could cause effective loss and transport of radiation belt electrons even in the absence of waves.

Dedication

To my family, whose unconditional love and support have made me who I am today.

Acknowledgements

I wish to begin by expressing my heartfelt gratitude to my advisor, Prof. Weichao Tu, who not only introduced me to this fascinating field but provided unparalleled guidance throughout my coursework, research, and career planning. Her wisdom illuminated my career trajectory during a challenging period of adjustment to life abroad and demanding graduate research. Her consistent encouragement and insightful direction were instrumental in initiating and sustaining my research, culminating in this dissertation. The valuable experiences and lessons she has imparted will continue to guide me through any hurdles I encounter in my research pursuits and life beyond. I extend my deep appreciation to my dissertation committee members, Profs. Paul Cassak, Piyush M. Mehta, and Earl Scime. Their valuable insights and unwavering support have significantly contributed to my academic journey. I am equally indebted to my fellow research group members – Xingzhi Lyu, Wondwossen Eshetu, Sang-Yun Lee, and Zhi Gu "Patrick" Li. The enlightening discussions, constructive advice, and unwavering camaraderie from you all have been truly beneficial. Finally, I wish to express my thanks to everyone who offered inspiration, guidance, and suggestions for each paper that has contributed to this dissertation. Your input has been crucial in shaping and refining my work.

Contents

Chapter

Figures

Figure

Chapter 1

Introduction

The Earth's magnetosphere, a tear-shaped cavity in space, is the result of the interaction between solar wind from the sun and the Earth's terrestrial magnetic field. Charged particles, trapped in the Earth's magnetosphere, form different plasma populations. Among these, the Earth's radiation belts – filled with trapped particles with energies ranging from ~100 keV to several MeV - pose potential threats to artificial spacecraft and astronauts in space. The electrons in Earth's outer radiation belt are highly dynamic; their fluxes can increase or decrease by several orders of magnitude within a few hours. As such, it is increasingly important to have a detailed and comprehensive understanding of the dynamics of radiation belt electrons, including the physical loss and source mechanisms.

Since the discovery of the radiation belts in 1959, decades of observations and research on various transport, source, and loss processes on radiation belts have greatly enhanced our understanding of the dynamics of radiation belt electrons. However, an anomalous loss mechanism called drift orbit bifurcation (DOB) is not yet fully understood. Traditionally, the effects of DOB on the transport of radiation belt electrons have been overlooked in modeling radiation belt dynamics. This dissertation primarily addresses this gap and focuses on the implementation of DOB effects in radiation belt dynamics simulations.

Chapter 2 commences with a discussion of the Earth's magnetosphere relevant to this work. I start with the structure of Earth's magnetosphere, and then describe the indices used to characterize geomagnetic storms. This is followed by a detailed description of Earth's radiation belts, the motions of charged particles, adiabatic invariants, and wave-particle interactions.

Subsequently, I introduce the dynamics of relativistic radiation belt electrons, including adiabatic effect, acceleration, and loss mechanisms. Chapter 2 concludes with a brief introduction of DOB and its significant impact on the transport of radiation belt electrons.

Chapter 3 presents our work of directly modeling the DOB effects on radiation belt electrons. I begin by introducing the guiding center test particle code we use to simulate the DOB effects. I then present the results of the simulation in various conditions using the T89c magnetic field model, including different geomagnetic conditions, initial equatorial pitch angles, starting points, electron bounce phases, and energy levels for both short-term and long-term transports. Both the traditional and nontraditional DOB are discussed. To quantify the long-term DOB transport, we calculate the diffusion coefficient of the second adiabatic invariant and of the radial distance from the Earth center at the midnight equator. Our results indicate that the long-term transport coefficients by DOB could be comparable to or even larger than those caused by wave-particle interactions, suggesting the importance of DOB effects on radiation belt electrons.

In Chapter 4, I introduce our study, which physically includes the effects of DOB in simulating the magnetopause shadowing loss of radiation belt electrons. We use a radial diffusion model with event-specific last closed drift shell (LCDS) values to simulate electron magnetopause shadowing loss. We first present three different methods for addressing DOB in the calculations of LCDS, which affect the loss term in the radial diffusion model associated with magnetopause shadowing. The traditional method is based on tracing magnetic field lines with a constant second adiabatic invariant, while the other two methods rely on guiding center test particle tracing, with one rejecting DOB, and the other including it. By implementing the LCDS from the three methods into the radial diffusion model, electron phase space density (PSD) and fluxes are simulated and compared with observations. We find that the radial diffusion model with event-specific LCDS

generally captures the features of magnetopause shadowing loss observed by Van Allen Probes. Moreover, the model that uses LCDS by tracing test particles and physically including DOB provides the best agreement with the data among the three methods.

Finally, we summarize our findings and discuss potential directions for future research in Chapter 5.

Chapter 2

Relevant Background

2.1 Earth's Magnetosphere

The Earth's magnetic field deflects the solar wind with supersonic plasma streams, forming a teardrop-shaped cavity around the Earth, which is called the Earth's magnetosphere. The boundary of the magnetosphere, the magnetopause, is defined by the balance of the solar wind dynamic pressure and the pressure of Earth's magnetic field. Its location can vary from a regular geocentric distance about 10 Earth radii (R_E) to extreme ones below about 6 R_E, depending on solar wind conditions. Meanwhile, the solar wind stretches the magnetosphere into a long magnetic tail (extending far beyond Earth-Moon distance) on the night side.

The magnetosphere is a cavity in the solar wind, but it contains abundant plasmas. The solar wind is an important source of the plasmas in Earth's magnetosphere, with another source being the Earth's ionosphere (Welling et al., 2015). Plasmas in the magnetosphere form various particle populations and current systems under the influence of the geomagnetic field, adding to the complexity of the magnetosphere, as illustrated in Figure 2.1 (Pollock et al., 2003). These generated current systems affect the geomagnetic field, and the strong perturbations of the geomagnetic field are called geomagnetic storms. To describe global storm levels, two indices, *Dst* and *Kp*, are commonly used.

The Disturbance Storm Time (*Dst*) index measures the energy intensity of the ring current. During geomagnetic storm times, more particles in the tail plasma sheet are energized and injected into the ring current, increasing its total energy. The ring current then causes a depression in the

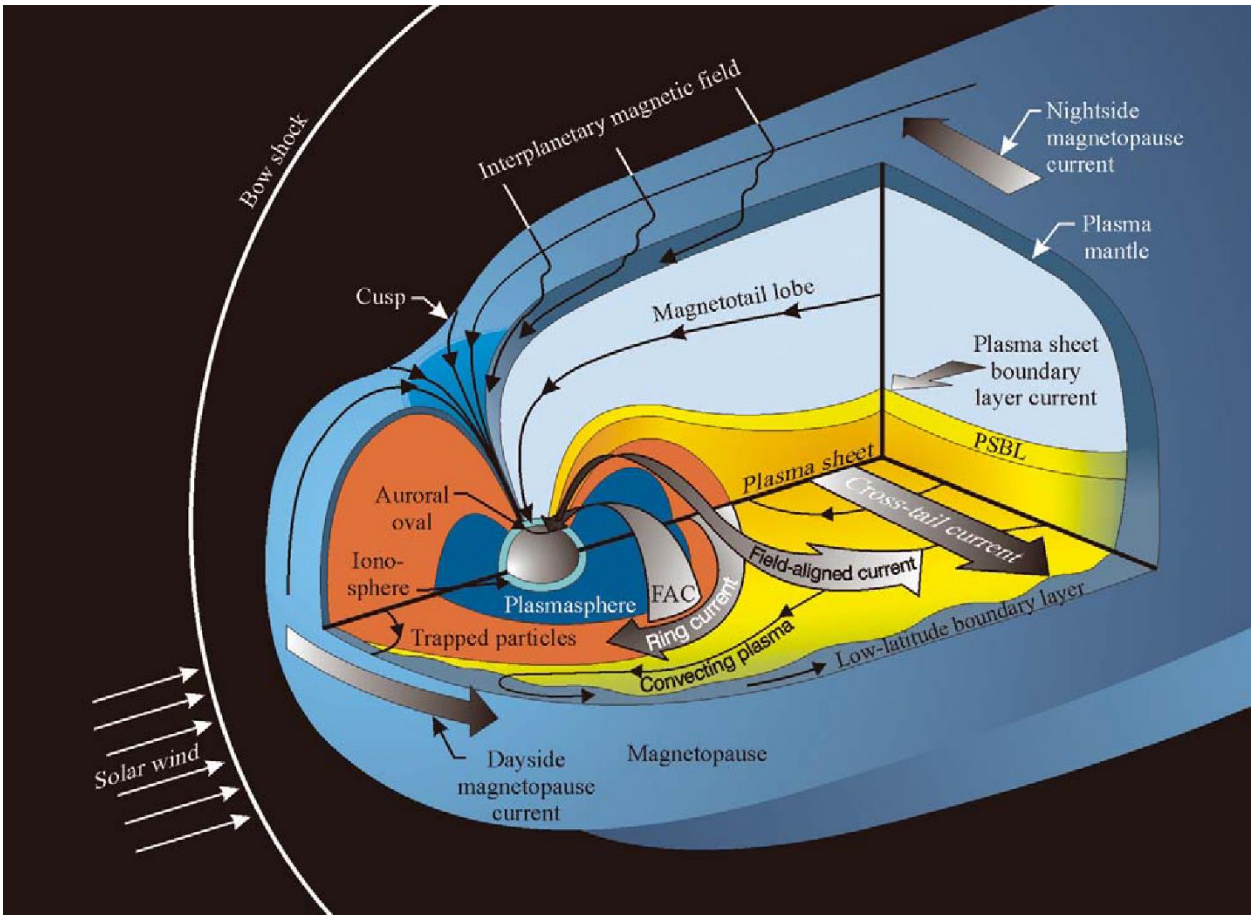

Figure 2.1: A schematic illustration of the Earth's magnetosphere. (Used with permission of Kluwer Academic Publishers, from Pollock, C., C:son-Brandt, P., Burch, J., et al. (2003). The Role and Contributions of Energetic Neutral Atom (ENA) Imaging in Magnetospheric Substorm Research. *Space Science Reviews*, *109*, 155–182; permission conveyed through Copyright Clearance Center, Inc.)

magnetic field at Earth's surface. *Dst* represents the averaged disturbance of the geomagnetic field on Earth's surface near the equator and is a weighted average value calculated hourly based on the measurements of the horizontal Earth's magnetic field component (H) from four low-latitude stations on Earth. Traditionally, geomagnetic storms are identified when the *Dst* index falls below -20nT (Gonzalez et al., 1994), with more negative *Dst* index corresponding to stronger storms. The SYM-H index is also used, which essentially mirrors the *Dst* index but with a higher time resolution of 1 min based on data from six low-latitude observatories. A typical geomagnetic storm has three characteristic phases: initial phase, main phase, and recovery phase (see Figure 2.2). A storm often commences with a significant positive SYM-H, known as storm sudden commencement. The initial phase, characterized by a positive SYM-H due to the enhanced magnetopause current, includes storm sudden commencement. When the SYM-H becomes negative, the main phase of the storm begins, and as the SYM-H continues to drop to very negative values, the ring current strengthens. The recovery phase begins when the SYM-H gradually increases to the pre-storm level and the ring current starts to recover.

The planetary *K* index, *Kp*, is another widely used index for geomagnetic activities. *Kp* is the average of 13 local *K* indices, each of which measures the disturbance of the horizontal component of Earth's magnetic field in a three-hour period at a specific mid-latitude observatory, with respect to a calm day. These measurements are then converted into a quasi-logarithmic scale from 0 to 9 with 1 indicating calm conditions and 5 or more indicating a geomagnetic storm. However, with a time resolution of 3 hours, *Kp* does not reflect rapid changes in magnetospheric dynamics.

Other than geomagnetic storms, there are more intermittent and brief disturbances of the Earth's magnetic field called geomagnetic substorms. These are significant for particle and energy

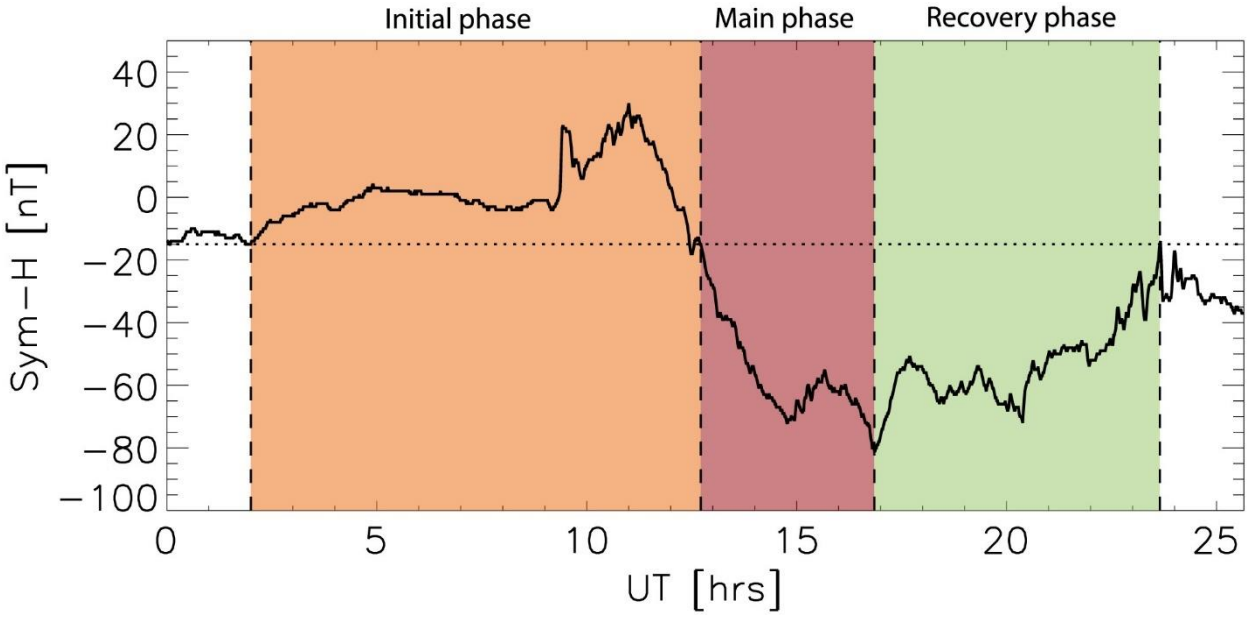

Figure 2.2: The initial phase (orange), main phase (red), and recovery phase (green) of a typical geomagnetic storm. (Reproduced from Walach and Crocott, 2019.)

injection from the tail plasma sheet into the inner magnetosphere. Both storms and substorms play important roles in the temporal and spatial evolution of the radiation belts. They are driven by strong solar wind and are caused by two main large-scale heliospheric structures: interplanetary counterparts of coronal mass ejections (CMEs), and stream interaction regions (SIRs) or co-rotating interaction regions (CIRs) of slow and fast solar wind flows (Koskinen & Kilpua, 2022).

2.2 Earth's Radiation Belts

The radiation belts occupy a region of space filled with energetic particles, extending from altitudes of a few hundred km to ~60,000 km above Earth's surface. They were first discovered as toroids of energetic protons and electrons surrounding the Earth by the Explorer 1 mission led by Dr. James Van Allen (Van Allen et al., 1958, 1959), leading to their alternate name: the Van Allen radiation belts. Our understanding of the dynamics of radiation belts has significantly evolved since their initial discovery. The radiation belts consist of two distinct belts separated by a slot region with depleted flux (see Figure 2.3). Typically, the inner radiation belt is located at L = 1.2 to 2 (where L or L-shell refers to the radial distance in Earth's radii at magnetic equator in a dipole magnetic field; it is also used for the near-dipole geomagnetic field and is widely used in space physics) and consists mainly of energetic protons. The outer radiation belt is located at L = 3 to 10 and consists mainly of energetic electrons. Due to the effects of geomagnetic storms and substorms on Earth's magnetosphere, the locations of the radiation belts are not fixed. However, the inner belt is much more stable than the highly dynamic outer belt, and the energies of the particles in the radiation belts can range from tens of keV to hundreds of MeV (Potapov, 2017). The typical energy levels are ~10s – 100s MeV for inner belt protons, ~10s – 100s keV for inner belt electrons, and ~0.1 – 10 MeV for outer belt electrons. Even the slot region can be temporarily filled with energetic electrons during geomagnetic storm times (Blake et al., 1992; Zhao and Li, 2013a, 2013b).

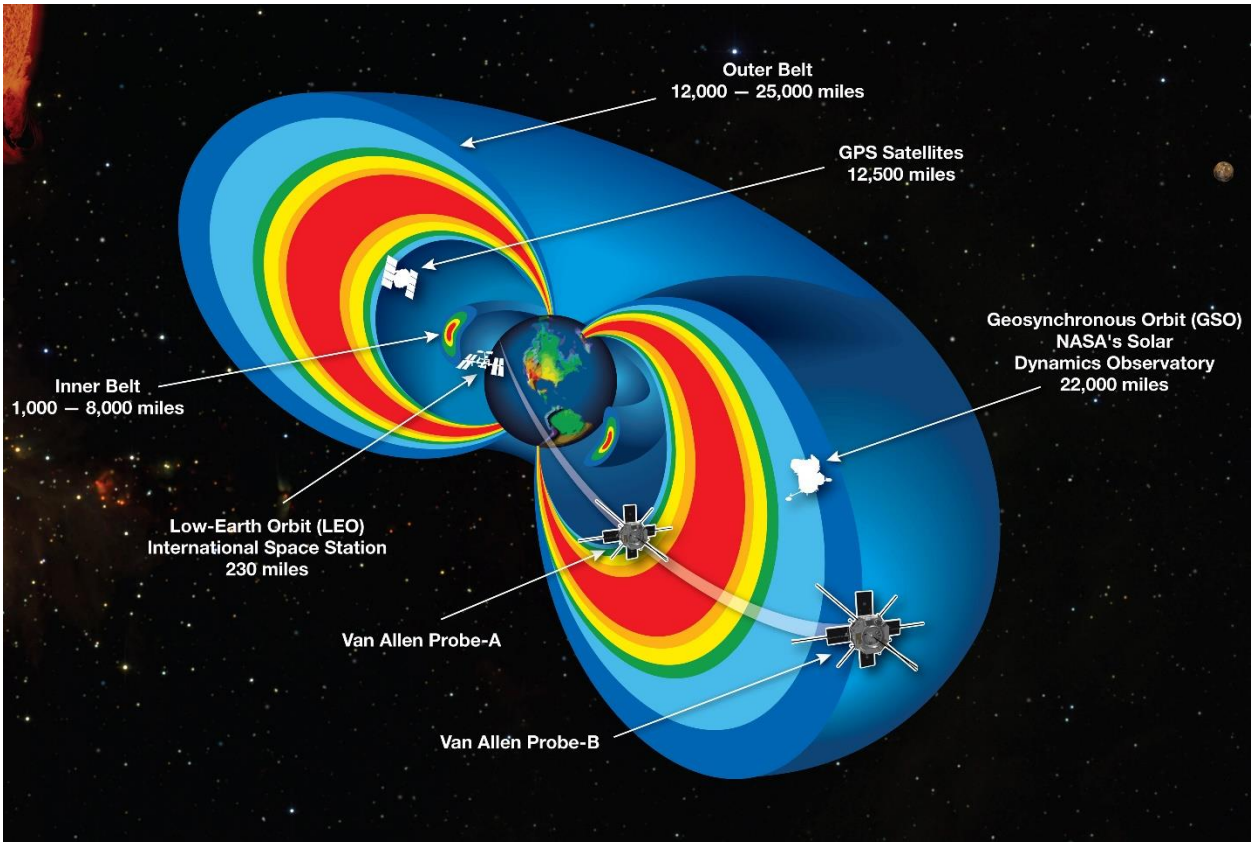

Figure 2.3: Schematic of radiation belts and satellite locations. The colors within the radiation belts represent the flux levels of the energetically trapped particles, increasing from blue to red. (Reproduced from https://www.nasa.gov/mission_pages/sunearth/news/gallery/20130228-radiationbelts.html, Credit: National Aeronautics and Space Administration.)

In Figure 2.4, fluxes of radiation belt electrons are represented as a function of both L-shell and time in the top panel, along with the hourly Dst index in the middle panel and solar wind velocity in the bottom panel. The figure clearly demonstrates that the outer belt is highly dynamic with variations on different timescales. Reeves et al. (2003) suggested that the effect of geomagnetic storms on radiation belt fluxes involves a delicate and complex interplay between particle acceleration and loss processes. According to their statistical study on 276 moderate and intense geomagnetic storms, only approximately half resulted in increased fluxes of relativistic electrons after the storms. A quarter led to decreased fluxes, while the remaining quarter caused little to no change in these fluxes. Understanding how the radiation belt electrons are accelerated and where they go during the fast dropout remain the most intriguing and outstanding questions in radiation belt studies.

2.3 Charged Particle Motions and Adiabatic Invariants

To study the dynamics of low-density plasma in Earth's magnetosphere, such as radiation belt electrons (10^{-6} cm^{-3}) and ring current protons (10^{-4} cm^{-3}) (Borovsky et al., 2020), the simplest approach is the single particle motion description. This method describes the motion of a particle under the influence of external magnetic and electric fields instead of the collective behavior of a plasma. Figure 2.5 shows the three distinctive motions of charged particles trapped on closed magnetic field lines. These are: gyromotion, bounce motion, and drift motion. These three motions happen simultaneously. Particles gyrate around the local magnetic field lines, bounce between the mirror points, and drift around the Earth (eastward for electrons, westward for protons). The time scales for these motions are distinct. Consider, for instance, a 1 MeV electron with an equatorial pitch angle of 60 degrees at a radial distance of approximately 6 R_E. The corresponding gyration,

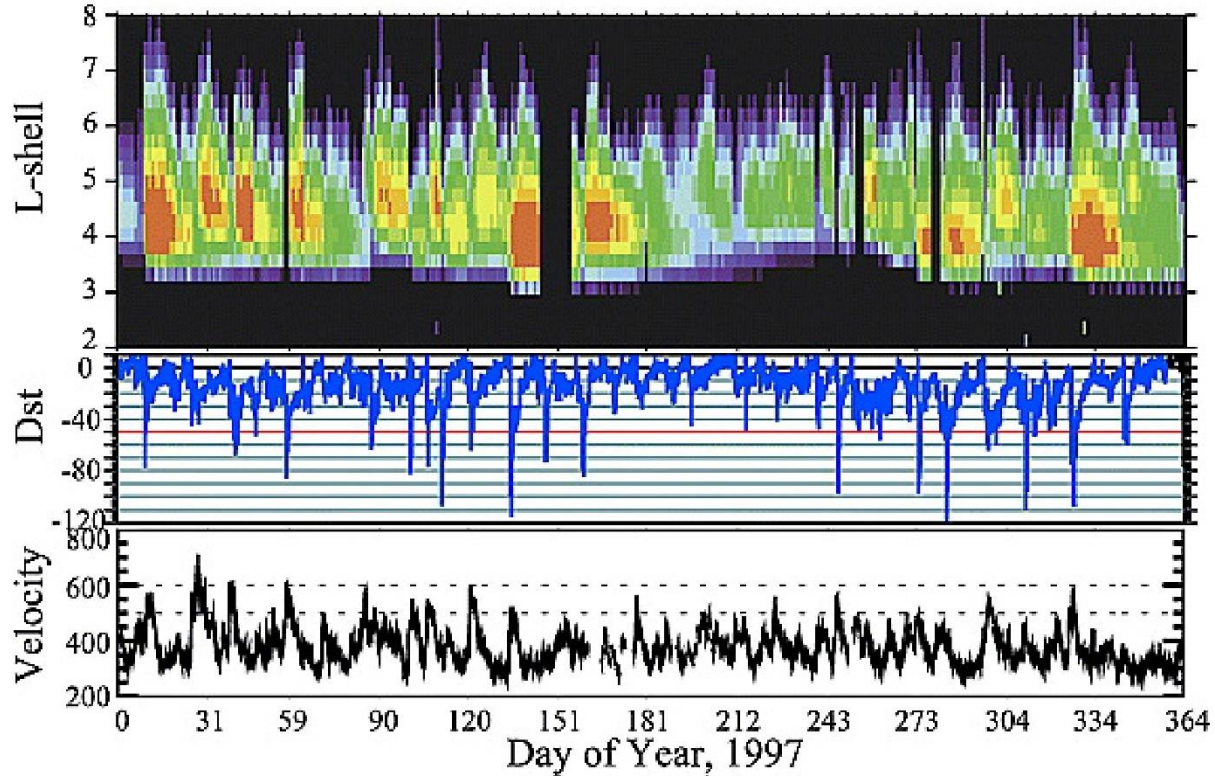

Figure 2.4: Fluxes of radiation belt electrons are represented as a function of both L-shell and time, along with the hourly *Dst* index and solar wind velocity. (Used with permission of American Geophysical Union, from Reeves, G. D., McAdams, K. L., Friedel, R. H. W., & O'Brien, T. P. (2003). Acceleration and loss of relativistic electrons during geomagnetic storms. *Geophysical Research Letters*, *30*(10), 1529; permission conveyed through Copyright Clearance Center, Inc.)

bounce, and drift periods for this electron would be about 10^{-3}, 10^{0}, and 10^{3} seconds, respectively. The pitch angle is the angle between the vector of the particle's velocity and the vector of the local magnetic field. Additionally, the particle flux distribution in relation to the pitch angle, also known as the pitch angle distribution (PAD), is an important characteristic for investigating particle dynamics. It could be used to indicate the physical processes occurring in a specific region, such as magnetopause shadowing, which will be discussed further in Section 2.4.3.

There are three adiabatic invariants corresponding to the three periodic motions. These adiabatic invariants are conserved if the fields vary slowly compared with the oscillation frequency of each motion, or the change of fields is over a length scale longer than the characteristic radius of the periodic motion related to the adiabatic invariant (Baumjohann & Treumann, 1996). The first adiabatic invariant is the magnetic moment associated with the gyromotion, which can be calculated as

$$\mu = \frac{p_{\perp}^2}{2m_0 B}, \tag{2.1}$$

where $p_{\perp}$ is the perpendicular component of the relativistic momentum of the particle with respect to the vector of the local magnetic field (with magnitude B), and m_0 is the particle's rest mass. The magnetic flux passing through the particle's gyromotion orbit is conserved if the first adiabatic invariant is constant. The second adiabatic invariant is the longitudinal invariant associated with the longitudinal bounce motion along the magnetic field line, which is given by

$$J = \oint p_{\parallel} ds = 2\sqrt{2m_0\mu} \int_{s_m}^{s_m'} \sqrt{B_m - B(s)}\, ds\,, \tag{2.2}$$

where $p_{\parallel}$ is the parallel relativistic momentum, ds is the elemental distance along the path of the guiding center (the center of the orbit related to gyromotion), s_m and s_m' are the two mirror points,

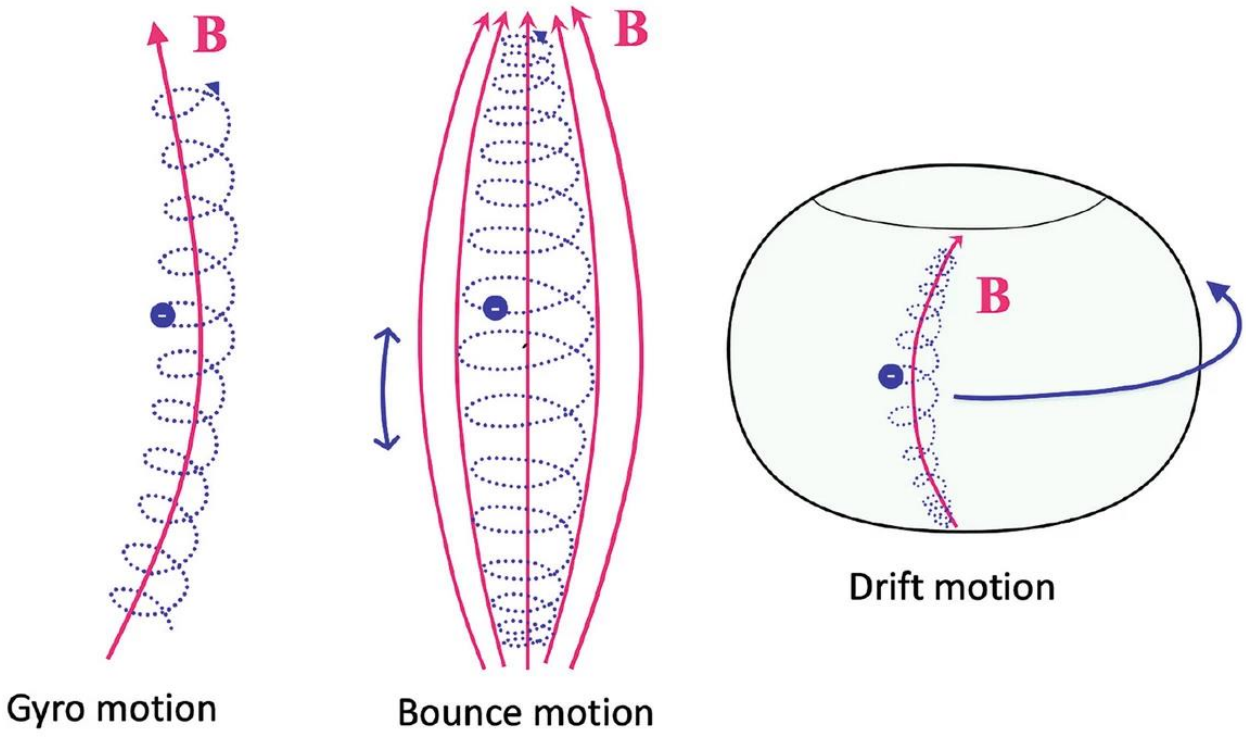

Figure 2.5: Three characteristic motions of an electron trapped on magnetic field lines. (Used with permission of Springer Nature, from Koskinen, H. E. J., & Kilpua, E. K. J. (2022). *Physics of Earth's radiation belts*. Springer International Publishing; permission conveyed through Copyright Clearance Center, Inc.)

and B_m and $B(s)$ are the magnetic field magnitude at the mirror point and local point s, respectively. To eliminate the dependence on particle momentum, K and I are used instead as the second adiabatic invariant, which are defined as

$$K = \int_{s_m}^{s_m'} \sqrt{B_m - B(s)}\, ds \tag{2.3}$$

$$I = \int_{s_m}^{s_m'} \sqrt{1 - B(s)/B_m}\, ds. \tag{2.4}$$

Note that I is no longer constant when there are external forces acting perpendicular to the magnetic field lines on the particle, while K and J remain conserved under adiabatic conditions (slow changes in the magnetic field and forces relative to the gyration period) (Roederer & Zhang, 2014). The third adiabatic invariant Φ is the magnetic flux enclosed by the drift shell of the particle, which is calculated as

$$\Phi = \oiint_S \vec{B} \cdot d\vec{S}, \tag{2.5}$$

where $\vec{B}$ is the magnetic field vector, and $d\vec{S}$ is the elemental cross section of the particle's drift shell. In 1970, Roederer suggested the Roederder L, as known as L^*, to associate the third adiabatic invariant Φ as

$$L^* = \frac{2\pi M}{|\Phi| R_E}, \tag{2.6}$$

where M is the Earth's dipole magnetic moment. L^* would be the same as L if the magnetic field is a dipole (Roederer, 1970). L^* can be referred to as the third adiabatic invariant since the conservation of L^* is equivalent to the conservation of the third adiabatic invariant. Apart from L^*

and L, the McIlwain L (or L_m) is also commonly used, which is calculated using a function between L_m, B_m, and I based on the dipole field. In a dipole field, $L^* = L_m = L$, while for non-dipole fields, L^* is the most physical parameter that identifies the drift shell of a particle.

Even in the case of low-density plasmas, solving the equation of motion for each individual particle is not only challenging but also impractical. Instead, kinetic theory, being the most developed theory in plasma physics, takes a statistical approach. It focuses on the evolution of the distribution function for a system of particles in phase space, under certain simplifying assumptions. In kinetic theory, the phase space density (PSD) represents the distribution function of particles in six-dimensional phase space and can be denoted as $f(x, y, z, p_x, p_y, p_z)$. Additionally, this function can evolve over time, leading to a time-dependent distribution, denoted as $f(x, y, z, p_x, p_y, p_z, t)$. It can also be written as $f(\mu, K, L^*, \phi_1, \phi_2, \phi_3, t)$ in terms of the three adiabatic invariants that characterize the radiation belt at a specific time point. ϕ_1, ϕ_2, and ϕ_3 represent the corresponding phases of the three periodic motions. Due to the limitation of radiation belt observations, the PSD commonly used in radiation belt studies is phase-averaged as $f(\mu, K, L^*, t)$. However, direct observation of the PSD is not possible; what we can observe is the electron flux, for example, the differential unidirectional flux $j(E_{ch}, \alpha, \vec{r}, t)$, where E_{ch} is the energy channel, α is the pitch angle, and $\vec{r}$ is the position. It is defined as the number of particles dN that cross a unit area dA perpendicular to the given incident direction per unit kinetic energy dE, unit solid angle $d\Omega$, and unit time dt, i.e., $dN = j(E_{ch}, \alpha, \vec{r}, t)dAd\Omega dEdt$. The PSD can then be obtained from flux using the relation $f = j/p^2$, where p is the momentum of the relativistic particles.

The adiabatic invariants are conserved when the environmental field changes slowly compared to each motion. However, they can be violated when the frequency of the field

approaches the oscillation frequency of their motions. The violation of adiabatic invariants can result in diffusion processes, leading to the transport of particles. Specifically, the violation of the three adiabatic invariants causes the energy diffusion, pitch angle diffusion, and radial diffusion processes, altering the particles' energy, pitch angle, and radial position. These diffusion processes smooth out the distributions of particles, contributing to the sources and losses of radiation belt electrons. Various waves, including Ultra-Low Frequency (ULF) waves, whistler mode chorus waves, plasmaspheric hiss waves (see Figure 2.6), lightning-generated Very-Low Frequency (VLF) waves, and VLF waves from man-made transmitters, can cause these diffusions through wave-particle resonance. For example, the resonant condition between magnetospheric waves and a particle's gyromotion is

$$\omega - k_{\parallel} v_{\parallel} = n\Omega/\gamma \,, \tag{2.7}$$

where ω is the wave frequency, $k_{\parallel}$ is the component of the wave vector parallel to the magnetic field, $v_{\parallel}$ is the parallel component of the particle's velocity to the magnetic field, n is an integer, Ω is the charged particle gyrofrequency and γ is the Lorentz factor. Additionally, there are other non-wave transport mechanisms that are not well understood, such as the Drift Orbit Bifurcation (DOB), which will be discussed later in Section 2.5.

2.4 Dynamics of Relativistic Radiation Belt Electrons

Earth's radiation belts contain energetic electrons and protons that present a hazardous radiative environment for spacecraft (e.g., Allen, 2010; Baker, 2001). The relativistic electrons in the radiation belts are characterized by large variations in flux on various time scales (Baker & Kanekal, 2008; Reeves et al., 2003). Recently, the NASA Van Allen Probes mission revealed two types of remarkable variations of outer belt electrons: the strong enhancement and the fast dropout

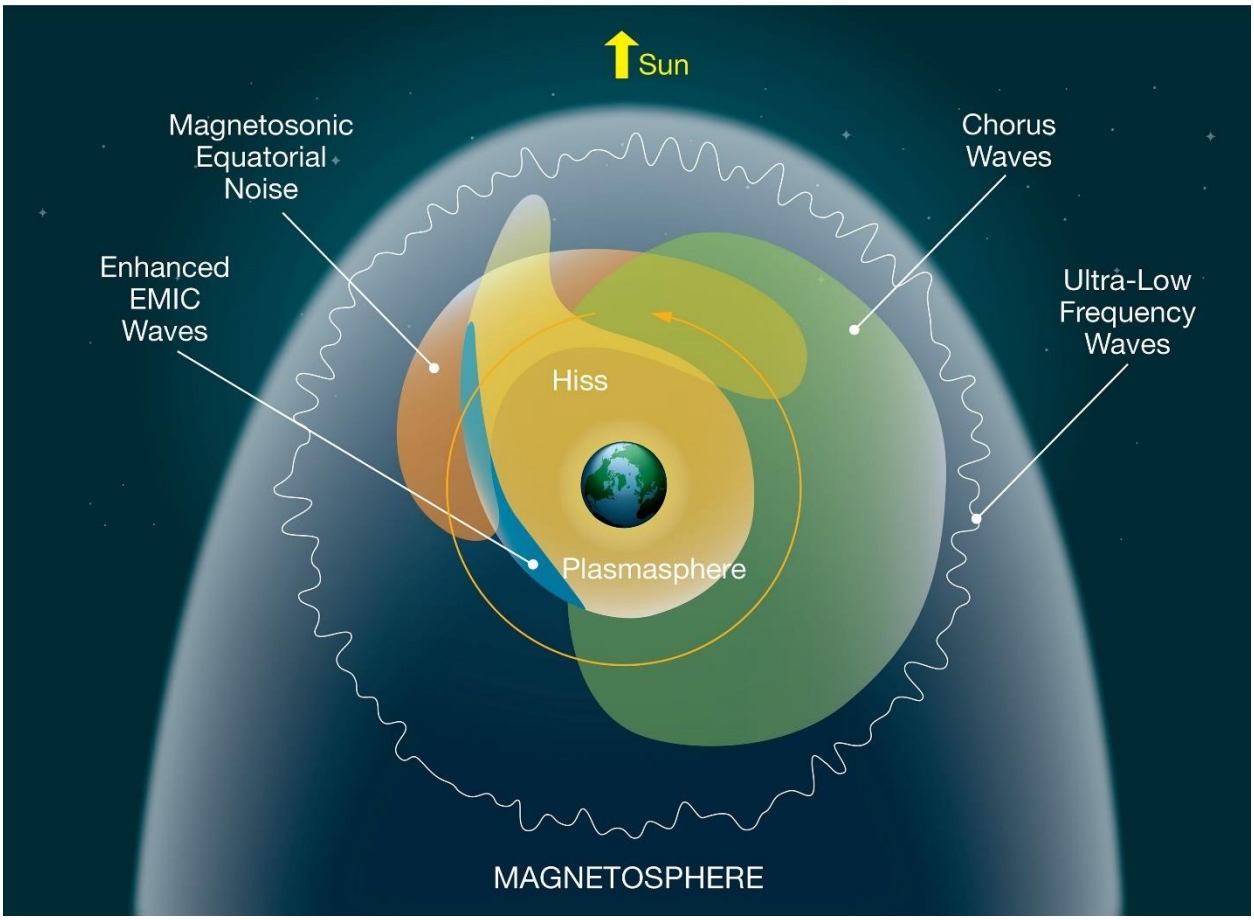

Figure 2.6: A schematic illustration of different types of plasma waves that affect relativistic electrons in Earth's radiation belts. The yellow circle around Earth is the electron drift path. (Reproduced from https://www.nasa.gov/feature/goddard/2019/in-solar-system-s-symphony-earth-s-magnetic-field-drops-the-beat, Credits: National Aeronautics and Space Administration's Goddard Space Flight Center/Mary Pat Hrybyk-Keith.)

of electron flux by orders of magnitude on timescales of a few hours (Thorne et al., 2013; Turner et al., 2012). The highly dynamic nature of Earth's outer radiation belt arises from the complex interplay of transport, acceleration (source), and loss processes affecting relativistic electrons. The transport of energetic electrons contributes to the source and loss processes resulting from the violation of the three adiabatic invariants.

2.4.1 Adiabatic effect

Transport can occur even when the adiabatic invariants are conserved, but the electrons can eventually return to their original status. This type of transport is known as the adiabatic effect (or *Dst* effect), which is a reversible process that can temporarily cause changes in the energy of electrons. For instance, during geomagnetic storms, the intensity of the ring current increases, leading to a negative *Dst* index and a decrease in the magnetic flux enclosed by the drift shell. In order to conserve the third adiabatic invariant, assuming that the change in the geomagnetic field is slower than the drift motion of the particles, the particles must move radially outward. As a result, the energy of the particles decreases to conserve the first adiabatic invariant as they move into regions of lower magnetic field. For a detector measuring particle flux at a fixed energy at a given location, it will observe an adiabatic decrease in particle flux if the slope of the particle energy spectrum is negative and the radial gradient of the PSD is outward positive (Kim and Chan, 1997). During the storm recovery phase when the magnetic field recovers, the particles then move radially inward and their energy gradually increases. The observed flux is restored gradually to its original level if the adiabatic effect is the dominant process. However, during storm times, various non-adiabatic transport mechanisms can act on electrons, leading to non-adiabatic and irreversible changes in electron flux. To eliminate the flux changes caused by the adiabatic effect and reveal the effects of non-adiabatic mechanisms, the electron PSD as a function of the three adiabatic

invariants are usually calculated based on the observed flux and utilized in studying the nonadiabatic acceleration and loss of radiation belt electrons.

2.4.2 Acceleration Mechanisms

Inward radial diffusion and local wave-particle acceleration are the two major acceleration mechanisms of radiation belt electrons.

When only the third adiabatic invariant is violated, the resulting radial diffusion can move electrons both inward and outward. In the case of inward diffusion (see Figure 2.7 (A)), to maintain the conservation of the first adiabatic invariant, the perpendicular energy increases to balance the increase in local magnetic field strength (Fälthammar, 1965; Schulz & Lanzerotti, 1974; Brautigam and Albert, 2000; Li et al., 2001; Barker et al., 2005). This inward radial diffusion, acting on a pre-existing PSD with an outward positive radial gradient, accelerates electrons (see Figure 2.7) and causes the pitch angle distribution to become more peaked around 90° as the perpendicular energy increases while the parallel energy keeps the same. Large-scale fluctuations in magnetic and electric fields in the magnetosphere contribute to this type of violation. These fluctuations, with frequencies comparable to the electron's drift frequencies, are defined as Ultra-Low-Frequency (ULF) waves (see Figure 2.6). Observations have shown a strong correlation between ULF waves and enhancements in MeV electron in the outer radiation belt (Baker et al., 1998a, 1998b; Nakamura et al., 2002). Furthermore, MHD simulations have highlighted the crucial role of ULF waves in the acceleration of relativistic electrons (Elkington et al., 1999; Hudson et al., 2000).

Local wave-particle acceleration (or in situ acceleration, local wave heating) is another important energetic electron acceleration mechanism through wave-particle interactions, which violates the first adiabatic invariant. Electrons can be accelerated through energy diffusion via

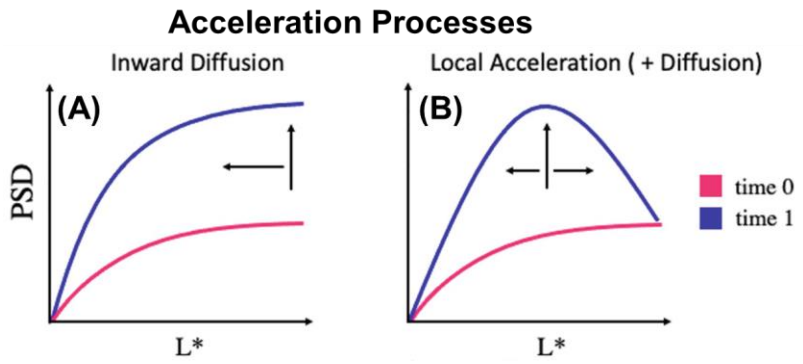

Figure 2.7: Illustration of the radial profiles of phase space density expected from (A) inward radial diffusion and (B) local wave-particle acceleration. (Used with permission of Springer Nature, from Koskinen, H. E. J., & Kilpua, E. K. J. (2022). *Physics of Earth's radiation belts*. Springer International Publishing; permission conveyed through Copyright Clearance Center, Inc.)

wave-particle resonance over multiple gyromotion periods. For example, outside the plasmasphere, whistler mode chorus waves have been proven effective in energizing energetic electrons to higher energies in the outer radiation belt, playing a significant role in the MeV electron flux enhancements (Horne & Thorne, 1998; Horne et al., 2005). Significant progress has been made in understanding the strong enhancement of relativistic electrons, which can be well reproduced by local acceleration from chorus waves, based on realistic wave and plasma conditions (e.g., Thorne et al., 2013; Tu et al., 2014b). Furthermore, fast magnetosonic waves have also been shown to be able to accelerate radiation belt electrons up to relativistic energies (Horne et al., 2007). Under local wave-particle heating, the PSD versus L^* profile typically exhibits a local peak at some L^* value (see Figure 2.7 (B)).

The two acceleration processes can occur simultaneously and the temporal and spatial coverage of PSD data from space missions are usually limited. These pose difficulties in distinguishing between the two acceleration mechanisms. For example, the local peak in the PSD versus L^* profile can also arise from a combination of radial diffusion and electron losses at high

L^*. Therefore, the relative importance of these processes still remains controversial (Brautigam & Albert, 2000; Chen et al., 2007; Jaynes et al., 2015; Reeves et al., 2013; Throne et al., 2010, 2013).

2.4.3 Loss Mechanisms

The dropout of radiation electrons is one of the most important and outstanding questions in radiation belt studies. Examples of observed fast dropouts of outer belt electrons are shown in Figure 2.8. During a fast dropout event, radiation belt electrons can be lost through two main mechanisms: transport across the magnetopause into interplanetary space, known as magnetopause shadowing, or by precipitation into the atmosphere.

Magnetopause shadowing loss occurs when the drift paths of electrons intersect with the magnetopause. This can happen either due to the compression of the magnetopause by the solar wind or the outward radial transport of electrons. During geomagnetic storm times, due to the *Dst* effect, the drift shell of electrons expands to conserve the third adiabatic invariant, resulting in outward transport. Outward transport can also be driven by radial diffusion due to ULF waves, which facilitate not only inward radial diffusion, but also outward radial diffusion (Fälthammar, 1965; Reeves et al., 1998; Shprits et al., 2006; Turner et al., 2012). During the outward radial transport, electrons decelerate due to the decreasing magnetic field strength at larger L values and the conservation of the first adiabatic invariant. Concurrently, the subsolar magnetopause is compressed closer to the Earth by the increased solar wind dynamic pressure, enhancing the electron losses to the magnetopause. Magnetopause shadowing loss is effective across a wide range of particle energies. More energetic electrons drift faster and are lost to the magnetopause sooner. Additionally, the loss is more effective for electrons with larger equatorial pitch angle due to the drift shell splitting effect (see Figure 2.9). Electrons start from nightside with larger equatorial

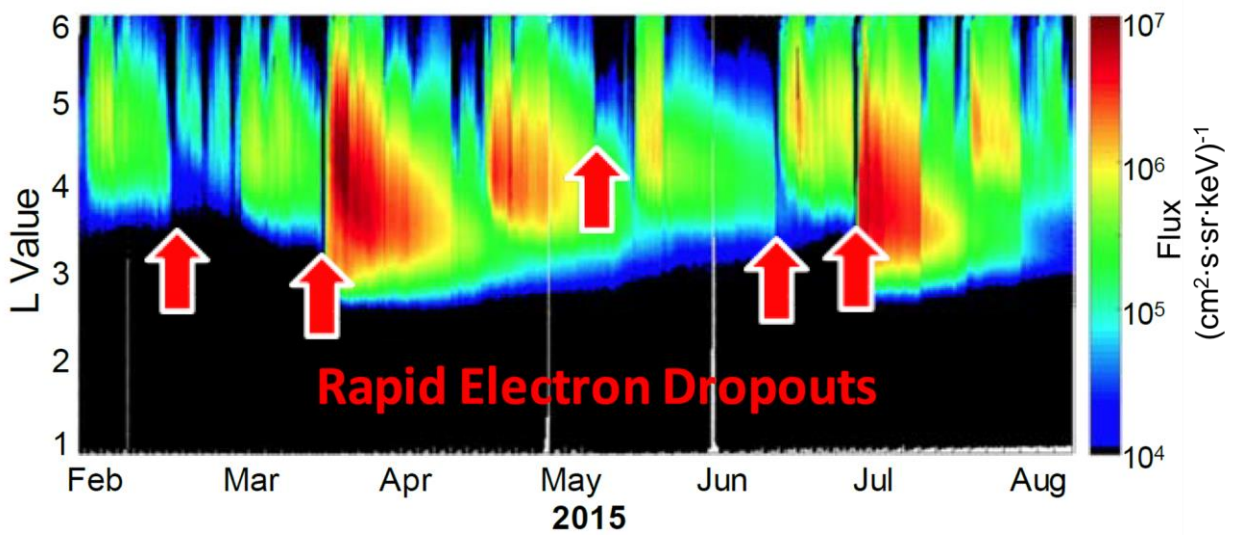

Figure 2.8: 1.8 MeV electron flux observed by Van Allen Probes.

pitch angles (smaller cosine values) drift further away from Earth on the dayside than those with smaller equatorial pitch angles (larger cosine values). Then electrons with larger equatorial pitch angle are more susceptible to loss through the solar wind compressed magnetopause. This leads to a butterfly-type electron pitch angle distribution at large *L*. The last closed drift shell (LCDS) has been widely used as a critical input in modeling magnetopause shadowing loss (Tu et al., 2014b, 2019; Yu et al., 2013) and evaluating electron loss (George et al., 2022; Olifer et al., 2018, 2021; Xiang et al., 2017). The LCDS is defined as the largest Roederer *L** (Roederer & Zhang, 2014) for drift shells that do not intersect with magnetopause or the open field lines.

Precipitation into the atmosphere is another important and complex non-adiabatic loss mechanism for radiation belt electrons. In the bounce motion of electrons, the mirror points are located closer to the Earth's atmosphere for smaller local pitch angles. When the pitch angles are small enough, electrons bounce into the atmosphere, collide with it, and are consequently lost. The change in particle pitch angle can result from wave-particle interactions. Precipitation is typically considered to result from wave-particle interactions that induce pitch angle diffusion of electrons (Thorne, 2010, and references therein). The waves that most commonly satisfy the wave-particle

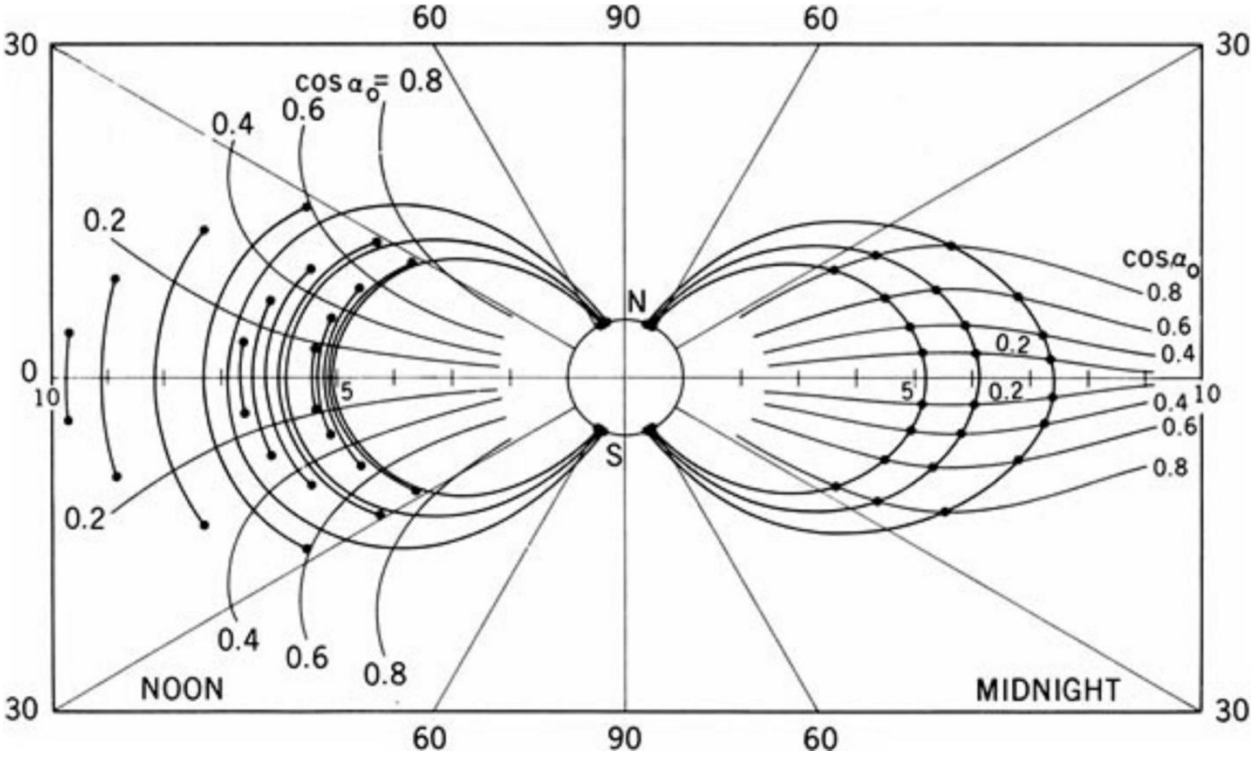

Figure 2.9: A schematic illustration of drift shell splitting from nightside to dayside. The dots are the mirror points corresponding to different equatorial pitch angle cosines. (Used with permission of Springer-Verlag Berlin Heidelberg, from Roederer, J. G., & Zhang, H. (2014). *Dynamics of magnetically trapped particles: foundations of the physics of radiation belts and space plasmas*. Astrophysics and space science library, Springer; permission conveyed through Copyright Clearance Center, Inc.)

resonance condition are electromagnetic ion cyclotron (EMIC) waves (Blum et al., 2013, 2015; Capannolo et al., 2019; Lyu et al., 2022; Meredith et al., 2003; Summers & Thorne, 2003; Shprits et al., 2016; Usanova et al., 2014; Zhang et al., 2016), chorus waves (Lorentzen et al., 2001; O'Brien et al., 2004; Shprits et al., 2007; Thorne et al., 2005), and plasmaspheric hiss waves (Abel & Thorne, 1998; Lyons et al, 1972; Lyons & Thorne, 1973; Meredith et al., 2006, 2007). Precipitation loss is generally more effective at smaller pitch angles, which are more easily decreased by wave-particle interactions to a pitch angle inside loss cone (electrons with local pitch angle inside loss cone are precipitated into the atmosphere). Note that many factors could affect the precipitation loss, such as the pitch angle diffusion rates can be different at different local pitch angle due to EMIC waves (Lyu et al., 2022). These factors are important in studies of loss mechanisms.

Even though there is a general understanding of the main loss mechanisms, the fast dropout of relativistic electrons has not been well studied, which remains as one of the most compelling and outstanding questions in Earth's radiation belt studies. Even though these traditional loss mechanisms discussed above have been extensively included in radiation belt models to simulate the fast electron dropouts, in many cases, the observed dropouts still cannot be fully explained (Albert, 2014, and references therein). For example, to simulate the rapid loss of MeV electrons across the entire outer belt during the October 2012 storm, Tu et al. (2014b) applied the DREAM3D diffusion model, which includes pitch angle diffusion, radial diffusion, and the event-specific last closed drift shell of electrons to physically account for the magnetopause shadowing loss. However, the simulated loss did not penetrate as deep in L^* as in the observations, and the large dropout at $L^* > 4$ was not sufficiently reproduced. Similarly, using a radial diffusion model with data-driven outer boundary and electron losses from wave scattering, Ozeke et al. (2017) well

explained the long-lasting (≥ 10 days) feature of the ultra-relativistic electron depletion in September 2014. However, the rapid electron dropout that initiated the long-term depletion remains unsolved. In many cases, the dropouts are observed to cover a wide range of L shells, electron energies, and pitch angles, which cannot be fully explained by even combining all the traditional mechanisms.

2.5 Drift Orbit Bifurcation of Electrons

Recent studies suggested that an anomalous process called drift orbit bifurcation (DOB), which was first discovered by Shabansky and Antonova (1968) and Shabansky (1972), can significantly affect the loss and transport of radiation belt electrons (e.g., Öztürk & Wolf, 2007; Ukhorskiy et al., 2011, 2014, 2015; Wan et al., 2010). DOB is a particle transport mechanism leading to the violation of the second and third adiabatic invariants, which is different from the mechanisms discussed since it is not caused by wave-particle interactions.

DOB occurs when the dayside magnetosphere is compressed by the solar wind, exhibiting two local magnetic field minima along a magnetic field line on either side of the equator (see Figure 2.10). The magnetic field strength distribution along the compressed field lines ($B(s)$, where s is the distance along the magnetic field line) shows a W-shape (Figure 2.10b-d) instead of a U-shape (Figure 2.10a, e). When particles traverse the dayside compressed W-shape region, that is, the bifurcation region (Öztürk & Wolf, 2007), they could be temporarily trapped in one of the hemispheres off the equator when the magnetic field strength at the local maximum at the equator is bigger than B_m, the magnetic field strength at the particle's mirror points. Particles will resume bouncing across the equator when they drift away from the bifurcation region. The first adiabatic invariant, μ, and B_m are constant during the DOB process. However, the second adiabatic

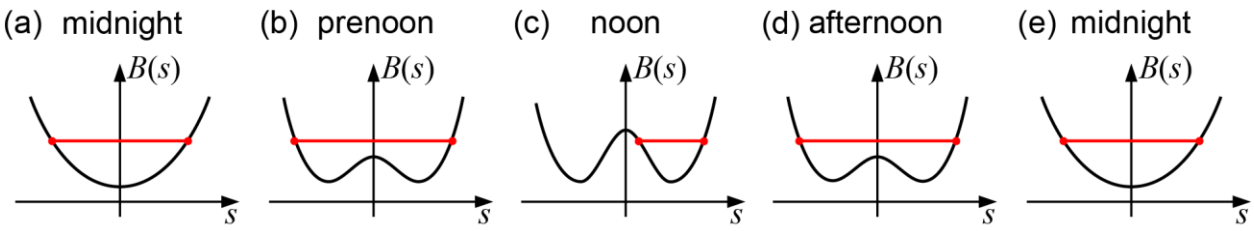

Figure 2.10: Illustration of drift orbit bifurcation (red lines) using magnetic field profiles from midnight to noon.

invariant, J or I, is violated when the particles are close to the bifurcation lines (Öztürk & Wolf, 2007), where the local B maximum at the equator is equal to B_m. I is usually used as the second adiabatic invariant of motion (rather than J) in a static magnetic field with no external electric field, as it is only related to the geometry of the magnetic field, and we will use I as the second adiabatic invariant in our study discussed in Chapter 3. During the DOB process, I is not conserved, and the drift shell is not closed. Moreover, since the changes of geomagnetic fields across the bifurcation lines are much faster than the drift period, the third adiabatic invariant, Φ or L^*, is undefined.

Many theoretical and numerical studies have been performed to quantify the change of the second adiabatic invariants due to DOB. For example, Öztürk and Wolf (2007) used the separatrix crossing theory (Cary et al., 1986) and theoretically derived the jump of the second adiabatic invariant, ΔI, at the bifurcations. Then by calculating the ensemble average of ΔI over particle bounce phases, they identified two regimes of particle transport: a diffusive regime, where $\langle \Delta I \rangle \approx 0$ and $\langle (\Delta I)^2 \rangle \neq 0$, for particles starting with large I values and a ballistic or advective regime, where $\langle \Delta I \rangle > 0$, for particles starting with small I values. For simplicity, their derivations are based on the north-south and east-west symmetry of the magnetic field. For the field lacking such symmetry, Wan et al. (2010) found much larger transport rates using a semi-numerical approach. On the other hand, since particles are subject to phase mixing after multiple bifurcations, it is critical to quantify the statistical invariant transport over many drift orbits. Ukhorskiy et al. (2011) performed test

particle simulations of DOB and found that the long-term evolution of I for electrons due to multiple DOB is a complicated interplay of both diffusion and advection processes.

The violation of both I and L^* during the DOB process can lead to radial transport of electrons for them to be lost through the magnetopause. For example, based on a 3D test particle approach, Ukhorskiy et al. (2014) found that the radial transport rates caused by DOB can exceed the transport rate driven by ULF waves by an order of magnitude. Later they applied a similar test particle code to simulate the global outer belt dropout observed during the March 2013 event (Ukhorskiy et al., 2015). Their results showed that DOB accounts for about 60% of the radial transport above $L = 5$, leading to fast loss to the magnetopause. Additionally, even though DOB is considered most efficient near the dayside magnetopause, Ukhorskiy et al. (2011) show that a broad range of outer belt drift shells is susceptible to DOB, even during quiet solar wind conditions. More recently, Desai et al. (2021) traced test particles in global magnetohydrodynamic (MHD) simulations to study the cross-field radial transport of relativistic electrons due to DOB. Their simulation results show that DOB can drive electron losses to the magnetopause and atmospheric loss cone and the convective electric field could make a significant effect on the long-term transport of electrons.

Chapter 3

Modeling the Effects of Drift Orbit Bifurcation on Radiation Belt Electrons

This chapter is based on the published paper: Huang, J., Tu, W., & Eshetu, W. W. (2022). Modeling the effects of drift orbit bifurcation on radiation belt electrons. *Journal of Geophysical Research: Space Physics*, *127*(11), e2022JA030827. https://doi.org/10.1029/2022JA030827.

3.1 Introduction

As discussed in Section 2.5, DOB has been suggested to significantly contribute to the loss and transport of radiation belt electrons. However, its effects have not been sufficiently explored and quantified. Moreover, the relative importance of DOB to the loss and transport of radiation belt electrons is not yet understood. To better understand the DOB effects, in this chapter we quantify electrons' short-term and long-term transport due to DOB under different geomagnetic conditions, which could be applied to global radiation belt modeling in the future. We also investigate the energy dependence of the electron DOB transport and the nontraditional DOB effects due to three local magnetic field minima which is reported here for the first time. Section 3.2 introduces the methodology and particle setup for the 3-D test particle simulations. Section 3.3 shows the simulation results for the short-term transport of electrons due to DOB after one full drift, including the nontraditional type of DOB effects due to three local B minima, and the long-term transport rates of electrons due to DOB after many drifts. Section 3.4 finishes with conclusions and discussions.

3.2 Test Particle Simulation

Since the first adiabatic invariant is conserved in DOB, we use the guiding center equations by Brizard and Chan (1999) to track the guiding center trajectories of electrons:

$$\begin{cases} \dfrac{d\vec{R}}{dt} = \dfrac{p_{\parallel}}{\gamma m}\dfrac{\vec{B}^*}{B_{\parallel}^*} + \dfrac{\mu}{\gamma q}\dfrac{\hat{b}\times\nabla B}{B_{\parallel}^*}, \\ \dfrac{dp_{\parallel}}{dt} = -\dfrac{\mu}{\gamma}\dfrac{\vec{B}^*\cdot\nabla B}{B_{\parallel}^*}, \end{cases} \tag{3.1}$$

where $\vec{B}^* = \vec{B} + (p_{\parallel}/q)\nabla\times\hat{b}$, $\hat{b}$ is the unit vector of $\vec{B}$, $\vec{R}$ is the electron guiding center position, $p_{\parallel}$ is the parallel momentum of the electron, γ is the Lorentz factor, m and q are the rest mass and charge of the electron, and μ is the first adiabatic invariant. These guiding center equations, which can be efficiently solved numerically and perform well in conserving the energy and adiabatic invariants of particles, have been widely used to investigate the effects of DOB on particles (e.g., Ukhorskiy et al., 2011, Wan et al., 2010). In our simulations, the fourth-order Runge-Kutta method is used to solve the guiding center equations numerically. Even though recent event or case studies of DOB utilized more recent Tsyganenko magnetic field models, such as the TS07D model (Tsyganenko & Sitnov, 2007) in Ukhorskiy et al. (2015), or global MHD fields with self-consistent electric fields (Desai et al., 2021), we have chosen the T89c magnetic field model (Tsyganenko, 1989) for simulations in this work. Both T89c and more recent Tsyganenko field models use a modular approach to include the various current systems that drive the field, with each current system parameterized by geomagnetic and/or solar wind parameters that is determined by long-term spacecraft field measurements (Tsyganenko, 2013). T89c model is utilized in this work since it is solely controlled by the geomagnetic *Kp* index, which makes the quantified transport rate of electrons (discussed in Section 3.3.3) easier to be parametrized for future application in global radiation belt models. Furthermore, the simulations are performed in static T89c magnetic field

conditions (i.e., given *Kp* levels) with no induced electric field to isolate the DOB effects due to magnetic field geometries. We are aware that more recent Tsyganenko models or global MHD models may more realistically represent the geomagnetic field conditions especially during intense storm events. But the focus of this study is to quantify the DOB-driven electron transport at static field conditions that could be easily applied to global radiation belt models and directly compared with other transport coefficients of radiation belt electrons which are also parameterized by the *Kp* index (e.g., Brautigam & Albert, 2000). In addition, we have set a zero-tilt angle of the Earth's intrinsic dipolar magnetic field in the GSM coordinates. The lower boundary of the model is set at 100 km altitude, which is the general height of the Earth's atmosphere. As there is no explicitly defined realistic magnetopause in the T89c magnetic field, we set the upper boundary as 20 times Earth's radius. If the radial distance of the particle's guiding center is out of the boundary, we assume the particle is lost.

In our simulations, we investigate the DOB effects at different geomagnetic conditions (*Kp* = 1, 3, 6) for electrons starting from various radial distances from Earth with different values of initial second adiabatic invariants (I_0), and at different energies (E = 1, 2, 4 MeV). The electrons' guiding centers are initiated from the midnight meridian with different L_M, which is the radial distance from Earth center to the midnight guiding center of the guiding magnetic field line at the magnetic equator, with unit of Earth radii. To further study the bounce phase dependence, the electrons' guiding centers are separated at a uniform distance along the initial guiding magnetic field line at midnight with a given L_M. These electrons are in different bounce phases with different local pitch angles but with the same equatorial pitch angles. Then we use the guiding center equations listed above to track the trajectory of each electron's guiding center. Our simulation

results for the short-term and long-term electron transport due to DOB are discussed in the next subsection.

3.3 Simulation Results

3.3.1 Traditional and Nontraditional DOB

For the short-term transport of electrons due to DOB, Figure 3.1 shows the distribution of the calculated second adiabatic invariant after one full drift of electrons from the simulations, I_1, versus the initial second adiabatic invariant, I_0, for electrons under different conditions. The initial equatorial pitch angle, α_{eq}, of electrons corresponding to the initial I_0 values are also denoted along the *x*-axis. Figure 3.1a is for 1 MeV electrons starting from the guiding field line at midnight with the initial radial distance at magnetic equator $L_{M0} = 6.8$ (where L_{M0} is the initial value of L_M) under $Kp = 3$. For each I_0 value 201 electrons with different bounce phases are simulated, with each black asterisk in the plot representing one electron. The results show that the electrons with different bounce phases can result in different changes of the second adiabatic invariant due to DOB. The thick red line shows the averaged value of I_1 over all the 201 electrons at different bounce phases, and the thin cyan line marks the $y = x$ line as a reference. Based on the simulation results, we calculate the change of the second adiabatic invariant, $\Delta I = I_1 - I_0$, for each electron and then the bounce averaged values of $\langle \Delta I \rangle$ and $\langle (\Delta I)^2 \rangle$ for all the electrons at the same initial I_0. As discussed in Section 2.5, previous results have shown that the short-term transport of electrons due to DOB can be identified as two regimes: a diffusive regime, with $\langle \Delta I \rangle \approx 0$, $\langle (\Delta I)^2 \rangle \neq 0$, for particles starting with large *I* values and a ballistic or advective regime, with $\langle \Delta I \rangle > 0$, for particles starting with small *I* values (Öztürk & Wolf, 2007). Our simulations results shown in Figure 3.1a

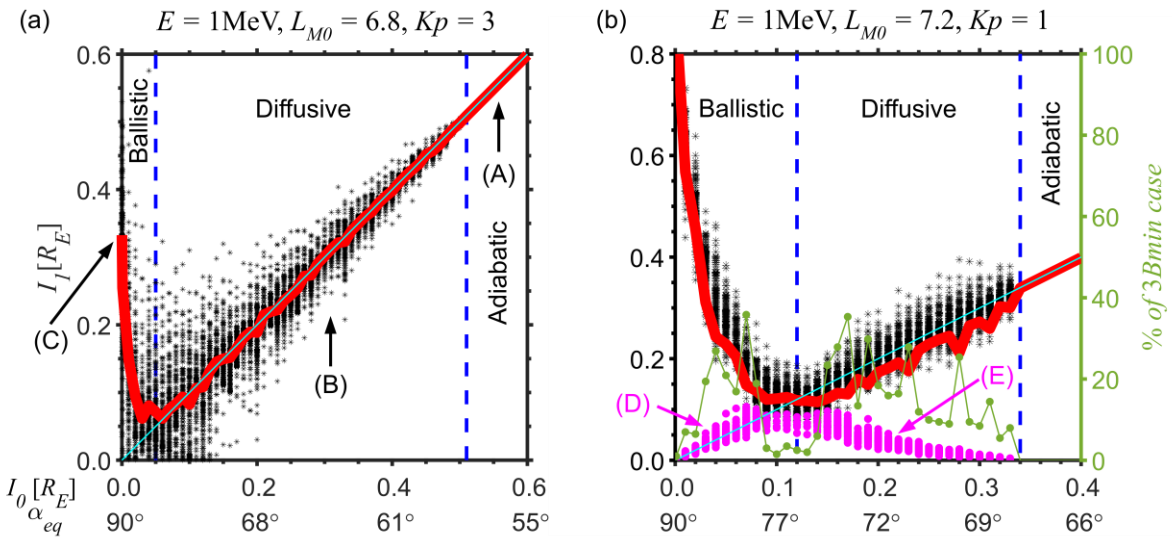

Figure 3.1: Distribution of the second adiabatic invariant after one drift for 1 MeV electrons starting from (a) L_{M0} = 6.8 at Kp = 3, and (b) L_{M0} = 7.2 at Kp = 1. The x-axes are the initial second adiabatic invariant values with corresponding initial equatorial pitch angles shown below. Left y-axes are the second adiabatic invariant values after one drift. The right y-axis of panel (b) is the percentage of the 3Bmin cases. The blue dashed lines are the boundaries for ballistic, diffusive, and adiabatic regimes. Marks (A-E) denote the different cases of electrons shown in Figure 3.2.

are consistent with the previous findings, with the red curve generally above the cyan $y = x$ line (i.e., $\langle \Delta I \rangle > 0$) at smaller I_0 and aligning with the $y = x$ line at larger I_0 values (i.e., $\langle \Delta I \rangle \approx 0$). Specifically, to define a clear cut between the ballistic and diffusive regions, we compare the values of $\langle \Delta I \rangle$ and $\langle (\Delta I)^2 \rangle$ by calculating the ratio of $\langle \Delta I \rangle / \langle (\Delta I)^2 \rangle^{1/2}$. As I_0 increases from 0 in the plot, we choose the first I_0 value with $\langle \Delta I \rangle / \langle (\Delta I)^2 \rangle^{1/2} < 50\%$ as the boundary between the ballistic and the diffusive regimes, as marked by the first dashed blue line in the plot. This definition works well to separate the ballistic and diffusive regimes in our simulation results, with more examples shown in Figure 3.5, which will be discussed in Section 3.3.2. Based on our simulation results, we can also mark the boundary between the diffusive and the adiabatic regimes as the second dashed blue line in the plot. The adiabatic regime is defined as the regime where no bifurcation occurs, as shown in the simulation results.

The results plotted in Figure 3.1a are consistent with previous findings of the short-term transport of electron I values due to DOB, which is called traditional DOB in this paper. To better illustrate the change of I during the electron's drift for traditional DOB, we select three cases to represent the electron transport in different regimes, as marked as (A), (B), and (C) in Figure 3.1a, and illustrate their DOB transport in Figure 3.2 panels (a-c). Each row of Figure 3.2 shows the change of magnetic field profiles along the field line, with the equator in the center, over one drift period of the electron, from midnight to prenoon, noon, afternoon, then back to midnight. The red lines represent the electron's mirror point magnetic field strength B_m, which are constant for each row during the electron's drift. The left-most column is the simulated guiding center trajectories for electrons of different initial conditions in each row. In Figure 3.2, we also include the field geometry at the two bifurcation points during the electron's drift. The first bifurcation point is

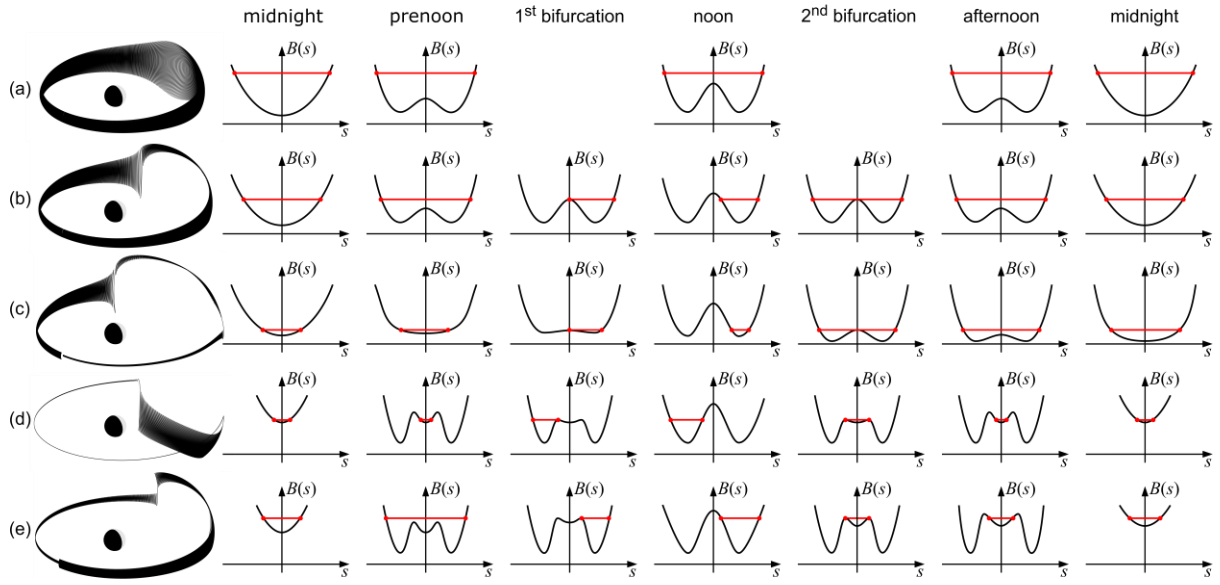

Figure 3.2: Traditional and nontraditional drift orbit bifurcation illustration with simulated particles' trajectories on the left-most and sketched B profiles along the drift on the right. (a-e) correspond to cases of (A-E) in Figure 3.1. The x-axis is the distance along the magnetic field line, and the y-axis is the magnetic field magnitude. The red lines are B_m values which are constant along the electron drift.

when the local B maximum at the equator increases to the level of B_m and the electron starts to bounce within one hemisphere off the equator, and the second bifurcation point is when the local B maximum at the equator drops to the level of B_m and the electron returns to bounce across the equator. These two bifurcation points can also be identified in the trajectory plots on the left-most. These plots in Figure 3.2 can help illustrate how the second adiabatic invariant changes due to DOB in each case. For example, for case (A) in Figure 3.1a, the electron has a small initial equatorial pitch angle (with large I_0), thus its B_m is big enough so that the local B maximum at the equator is always smaller than B_m as shown in Figure 3.2a, leading to no bifurcation and the electron motion is adiabatic. As the initial equatorial pitch angle increases, for example, case (B) in Figure 3.1a, B_m becomes smaller, and the local B maximum can be bigger than B_m as shown in Figure 3.2b. This leads to bifurcation as shown in the red line between the 1st and 2nd bifurcation points and the trajectory plot on the left. For this case, the second adiabatic invariant does not change much after the bifurcation, corresponding to the diffusive regime in Figure 3.1a. However, when the initial equatorial pitch angle is even bigger, and the electron is mirroring near the equator, like case (C) in Figure 3.1a, the second adiabatic invariant shows a ballistic jump after the bifurcation as shown in Figure 3.2c. This jump is consistent with the separatrix crossing theory proposed by Cary et al. (1986).

So far, we have discussed the traditional DOB transport in our simulation results that are consistent with previous findings. On the other hand, we find that under certain conditions, electrons can undergo nontraditional DOB transport, which is reported here for the first time. Back to Figure 3.1, in panel (b), we plot the change of I for electrons with E = 1 MeV, L_{M0} = 7.2, and Kp = 1. In addition to the ballistic, diffusive, and adiabatic regimes of electrons shown by black asterisks similar to the traditional DOB in panel (a), there are two distinct populations of electrons

marked as magenta dots in panel (b), which show different transport in I and are identified as nontraditional DOB transport. Specifically, we find that the electrons marked in magenta include one population of electrons showing diffusive transport with $\langle \Delta I \rangle \approx 0$ in the traditional ballistic regime, and another population showing ballistic transport with $\langle \Delta I \rangle < 0$ in the traditional diffusive regime. These electrons undergoing nontraditional DOB share the same I_0 values as the electrons with traditional DOB but are of different bounce phases, which is interesting. To illustrate the statistical significance of the nontraditional DOB cases, in Figure 3.1b, we plot the percentage of electrons with nontraditional DOB at each I_0 value in the green curve, with a corresponding y-axis on the right. We see that the percentages of nontraditional DOB cases are generally low, mostly below 20% for all the I_0 values. This explains why the bounce averaged I transport curve in panel (b), the thick red curve, looks similar to that in panel (a) for the pure traditional DOB case, since it is still statistically dominated by the electrons undergoing traditional DOB transport. Therefore, the nontraditional DOB could have a minor effect on the statistically averaged transport of electrons, but its distinct transport is still new and interesting.

To explore the mechanism for the nontraditional DOB transport, we select two cases of electrons marked by (D) and (E) in Figure 3.1b and plot their evolution of B profiles along the electron drift in Figures 3.2d and 3.2e, respectively. The interesting thing we find is that the nontraditional DOB cases are caused by three local B minima of the magnetic field strength rather than two local B minima for the traditional cases. The third B minimum near the equator is generally much shallower than the two B minima off the equator, as shown in Figures 3.2d and 3.2e. When the electrons are trapped around the third B minimum after the 2nd bifurcation point, its second adiabatic invariant will be small, leading to a diffusive change for electrons with initially

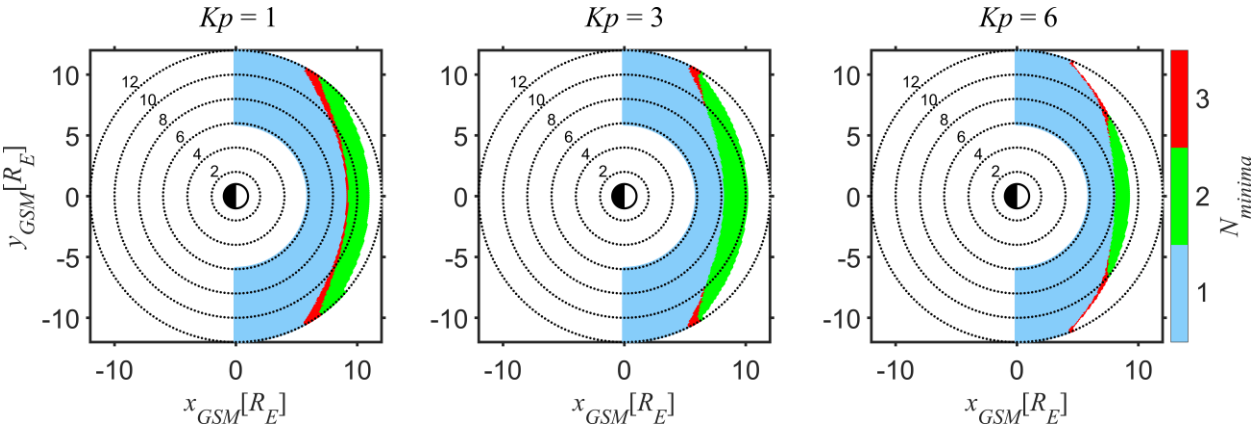

Figure 3.3: Number of magnetic field minima for field lines crossing the magnetic equator between $L = 6$ and $L = 12$ on the dayside for the T89c magnetic field model at (a) $Kp = 1$, (b) $Kp = 3$, and (c) $Kp = 6$. Blue, green, and red areas are regions with field lines of one, two, and three local B minima, respectively. The white area on the dayside inside $6 \leq L \leq 12$ are regions with open field lines.

small I_0 values (e.g., case (D)) and a ballistic jump for electrons with initially big I_0 values (e.g., case (E)).

The three local B minima in the magnetic field models have been reported a long time ago (e.g., Alekseev & Shabansky, 1972; Roederer, 1969), but its effect on the particle DOBs is reported here for the first time. To better illustrate the magnetic field geometry in the T89c magnetic field model, in Figure 3.3, we trace magnetic field lines from the magnetic equator from $L = 6$ to 12 on the dayside and plot the number of B minima on the GSM x-y plane. The blue area is where field lines are identified with one B minimum, the green area is the region with field lines of two local B minima, and the red area is for field lines with three local B minima. The white area on the dayside at $6 \leq L \leq 12$ are regions with open field lines. Bifurcation can occur in both the red and green areas. Interestingly, results in Figure 3.3 show that the three local B minima regions (red areas) are located between the single B minimum and two local B minima regions (between blue and green). Moreover, for $Kp = 1$, the red three B minima area covers all the transition region from the single B minimum to two B minima regions (blue to green), which means the electrons must

cross the three local *B* minima region before entering the two local *B* minima region. This explains why in Figure 3.1b at *Kp* = 1, the nontraditional DOB cases due to three *B* minima cover all the I_0 values. While for *Kp* = 3, the results in Figure 3.3 show that there are regions with no three *B* minima cases in between blue and green, suggesting that for certain values of L_{M0} and I_0 there will be cases with no three *B* minima effects, as shown in the case of Figure 3.1a. With the distribution of three *B* minima regions shown in Figure 3.3, we could also expect the nontraditional DOB effects due to three *B* minima to be more significant at larger L_{M0} values and for smaller I_0. This is because particles with smaller second adiabatic invariant or bigger equatorial pitch angle drift further out on the dayside due to the drift shell splitting effect (Roederer, 1967). This *Kp*, L_{M0}, and I_0 dependence of the three *B* minima effects on nontraditional DOB is further demonstrated in the simulation results shown in Figure 3.5, which will be discussed in the next subsection.

3.3.2 L_M, *Kp*, and *E* Dependence of the Short-Term DOB Transport

Simulation results in Figure 3.1 have shown that the short-term transports of electrons due to DOB are distinct under different conditions. Here we further investigate the L_M, *Kp*, and *E* dependence of the short-term DOB transport of electrons over one drift. Figure 3.4 shows the trajectories of 1 MeV electrons on the GSM X-Y plane in the T89c magnetic field model. These electrons are launched at midnight on the equator with ($5 \leq L_{M0} \leq 10$, spacing $\Delta L_{M0} = 0.2$) of 89° equatorial pitch angles and at *Kp* = 1, 3, 6, respectively, in the three panels. The black curves correspond to stably trapped particles, the blue curves indicate bifurcating trajectories, and the green curves are the particles that reach the simulation outer boundary $r = 20\ R_E$ before completing one full drift or untrapped particles. The dashed red circle represents the geosynchronous orbit.

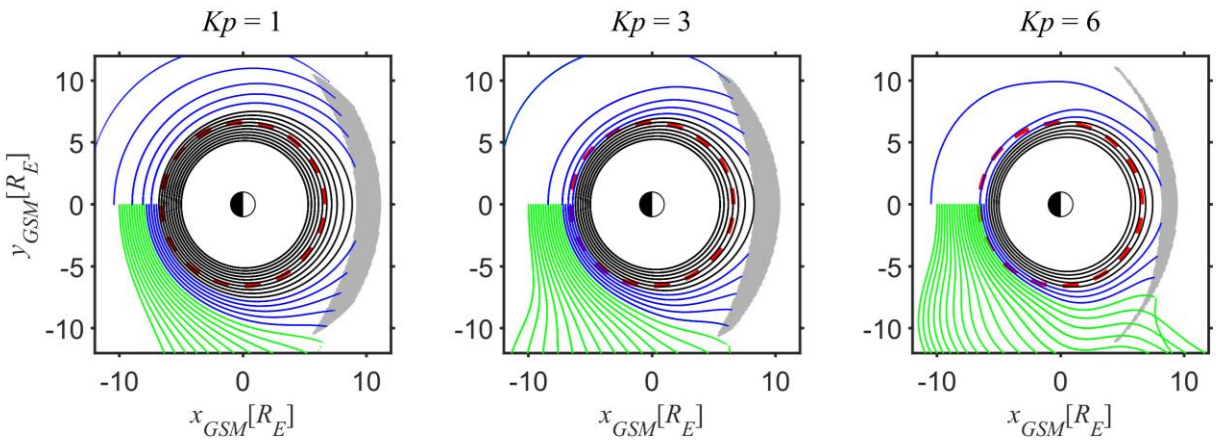

Figure 3.4: Trajectories of electrons starting from $5 < L_{M0} < 10$ with $\Delta L_{M0} = 0.2$ on the midnight magnetic equator with 89° equatorial pitch angle at (a) $Kp = 1$ (a), (b) $Kp = 3$, and (c) $Kp = 6$. The black curves represent the stably trapped electrons. The blue curves are bifurcated drift shells. The green curves indicate the untrapped electrons, which reach $r = 20\ R_E$ before completing one full drift. The gray area on the right for each panel is the region with two or three local B minima along the field lines, corresponding to the red and yellow areas in Figure 3.3. The dashed red circle is the geosynchronous orbit.

The gray areas are the regions with at least two B minima along the field lines, that is, the green and red areas in Figure 3.3. Trajectories in Figure 3.4 show that the bifurcating trajectories (blue curves) or DOB effects move closer to Earth as Kp increases, penetrating inside the geosynchronous orbit for $Kp \geq 3$, which indicates that DOB can affect a broad region of the outer radiation belt electrons. In addition, the bifurcating trajectories in blue show that the L_M values of electrons can show a big outward jump after one drift. This is corresponding to the jump of I at small I_0 values shown in the ballistic regimes in Figure 3.1. Since B_m is constant during DOB (conservation of the first adiabatic invariant), a ballistic jump in I value will directly lead to a ballistic jump in L_M, resulting in the outward radial transport of electrons. More analysis on the electron transport in L_M will be discussed in Figure 3.6 and therein.

To investigate the L_M and Kp dependence of the short-term I transport due to DOB, in Figure 3.5, we plot the simulation results with different L_{M0} values of $L_{M0} = 6.4$, 6.8, and 7.2, and

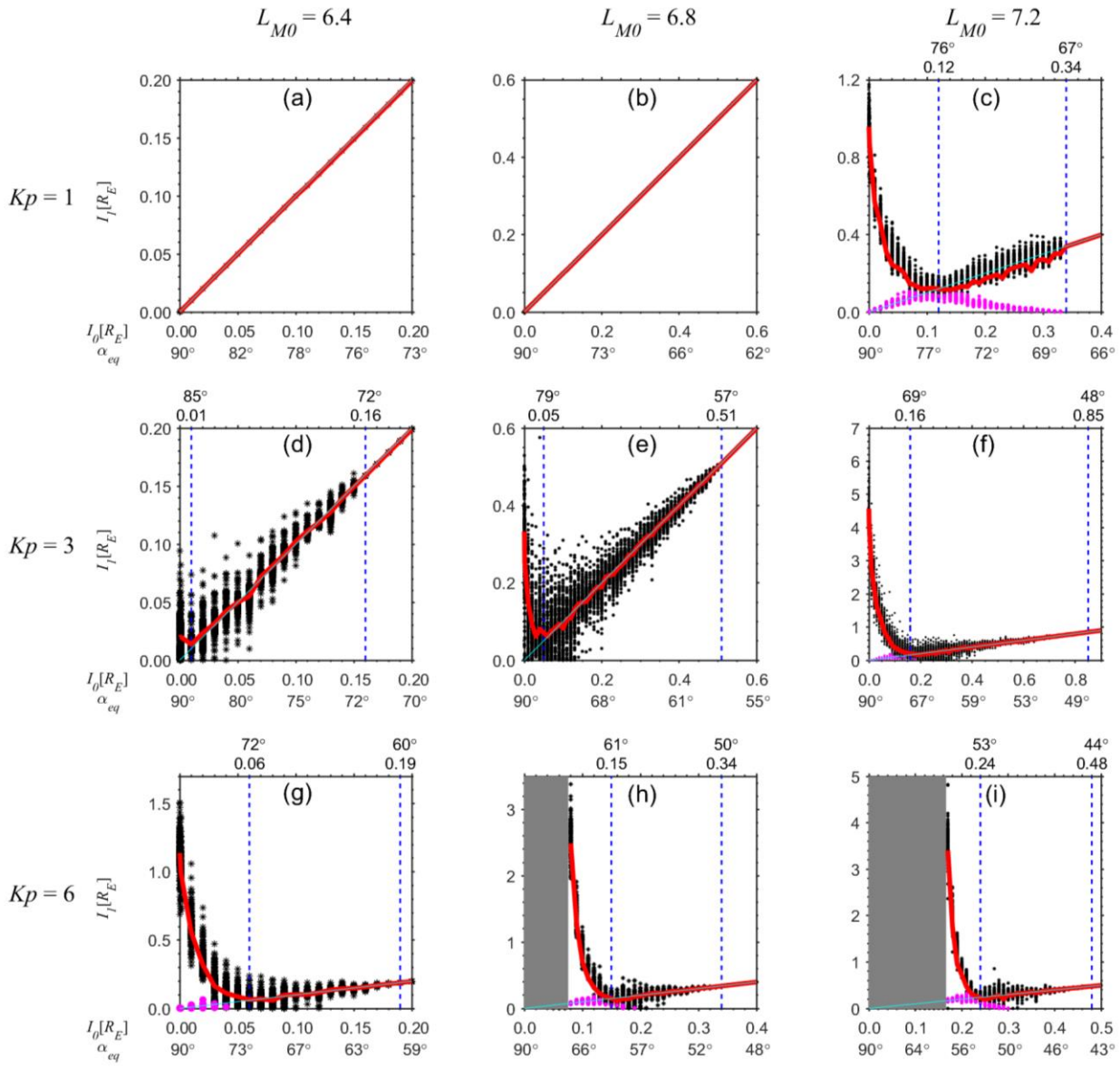

Figure 3.5: Same format as Figure 3.1 but for Kp = 1 (a-c), Kp = 3 (d-f), Kp = 6 (g-i), and L_{M0} = 6.4 (a, d, g), L_{M0} = 6.8 (b, e, h), L_{M0} = 7.2 (c, f, i). The values above the dashed blue lines are the corresponding values of initial second adiabatic invariants and initial equatorial pitch angles at the boundaries.

at different *Kp* levels of *Kp* = 1, 3, and 6. The format of each panel is the same as in Figure 3.1. The blue dashed lines separate the ballistic, diffusive, and adiabatic regimes from left to right, with the corresponding values of initial second adiabatic invariants and initial equatorial pitch angles at the boundaries denoted on top. The grey areas are for untrapped electrons which reach $r = 20\ R_E$ before completing one full drift, like the green curves in Figure 3.4. Results in Figure 3.5 suggest that at a given *Kp* value, DOB effects are more significant at larger L_{M0}. At *Kp* = 1, there is no DOB at L_{M0} = 6.4 and 6.8 (consistent with the results in Figure 3.4), but the traditional and nontraditional DOB transport becomes effective at L_{M0} = 7.2. For *Kp* = 3 and 6, we see that the I_0 range for DOB effects, that is, up to the I_0 value of the second blue dash line, is wider as L_{M0} increases. Additionally, the ballistic jump in *I* due to DOB in the ballistic regime is bigger at higher L_{M0}. Moreover, the simulation results also demonstrate that the DOB transport gets more significant as *Kp* increases. First, the L_M coverage of DOB approaches closer to Earth at higher *Kp* values, for example, DOB is effective at L_{M0} = 6.4 for *Kp* > 3 but not for *Kp* = 1. Also, at a given L_{M0}, the ballistic jump in *I* in the ballistic regime is generally larger as *Kp* increases. For the nontraditional DOB transport marked in magenta dots, we see that it only affects the high L_{M0} region at *Kp* = 3, which is consistent with the coverage of the three *B* minima region plotted in Figure 3.3. Also, the nontraditional DOB effect due to three *B* minima is more effective at smaller I_0 values (or larger equatorial pitch angles) for *Kp* = 3 and 6 due to the drift shell splitting effects as discussed in Section 3.1 with Figure 3.3.

In addition to the electron transport in *I*, it is also useful to investigate the radial transport of electrons in L_M due to DOB, as shown in the example trajectories in Figure 3.4. Following the format of Figure 3.5, we calculate the change of L_M for electrons after one drift at different conditions and plot the results in Figure 3.6. The *x*-axes are identical to Figure 3.5, but now the *y*-

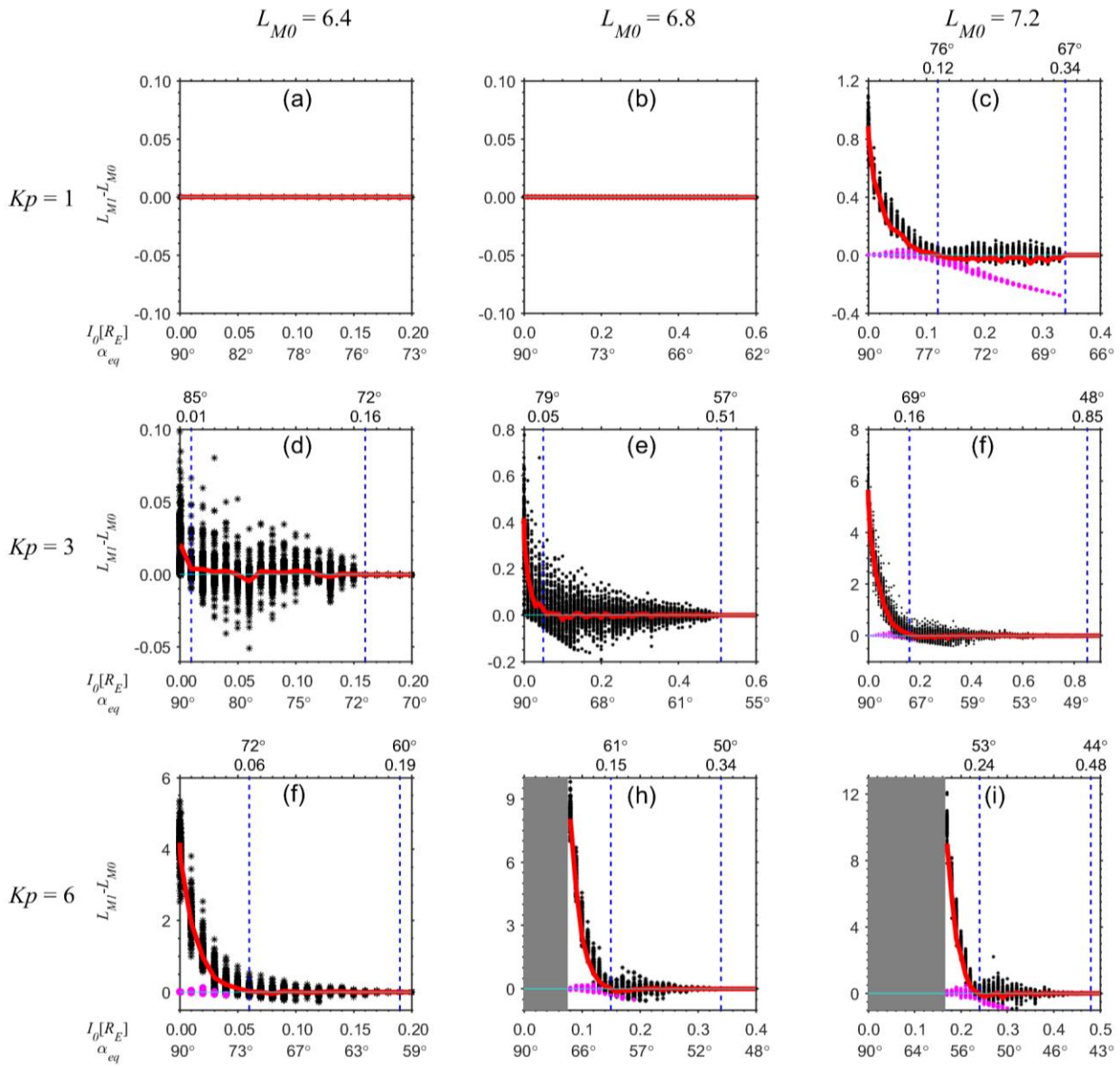

Figure 3.6: Same format as Figure 3.5, but with *y*-axis showing the change of L_M after one full drift.

axis is showing the change in L_M, that is, $L_{M1} - L_{M0}$, where L_{M1} is the L_M value of the electron after it returns to midnight after one full drift. The thick red curves now represent the bounce-averaged change of L_M, $\langle \Delta L_M \rangle$ with $\Delta L_M = L_{M1} - L_{M0}$, over one drift. Since I has a one-to-one correspondence with L_M due to the constant B_m, the patterns of the radial L_M transport in Figure 3.6 is similar to those of I transport in Figure 3.5, showing the same ballistic (with $\langle \Delta L_M \rangle > 0$), diffusive (with $\langle \Delta L_M \rangle \approx 0$), and adiabatic regimes, similar transport due to nontraditional DOB effects, as well as similar L_{M0} and Kp dependence in the transport. It is worthwhile to point out that the jump in L_M due to DOB can be quite significant for high equatorial pitch angle electrons in the ballistic regime, for example, at Kp = 3 with $\langle \Delta L_M \rangle$ reaching ~ 6 R_E at L_{M0} = 7.2 and at Kp = 6 with $\langle \Delta L_M \rangle$ reaching 4 R_E even closer to Earth at L_{M0} = 6.4. This further demonstrates that DOB can play a significant role in the particle transport in the inner magnetosphere.

Even though energy is conserved during the DOB process in a static magnetic field, the electron transport in I and L_M due to DOB can be energy-dependent. Based on the separatrix crossing theory in Cary et al. (1986) and the analytical and numerical calculations in Öztürk and Wolf (2007), the DOB transport is expected to be more significant at higher particle energies, which is related to the energy-dependent gyroradius of electrons at the mirror point. This is consistent with our simulation results shown in Figure 3.7, which plots the distribution of I_1 after one drift versus initial I_0 for electrons with L_{M0} = 7.2, Kp = 1 but at different energies of 1, 2, and 4 MeV respectively. The DOB effects are found to be more significant as the energy increases. For example, the ballistic jump in I at small I_0 values is generally larger at higher energies. Also, at a given I_0 value, there is a wider spread in I_1 over different bounce phases as electron energy increases, which is also consistent with the analytical results in Öztürk and Wolf (2007). Note that

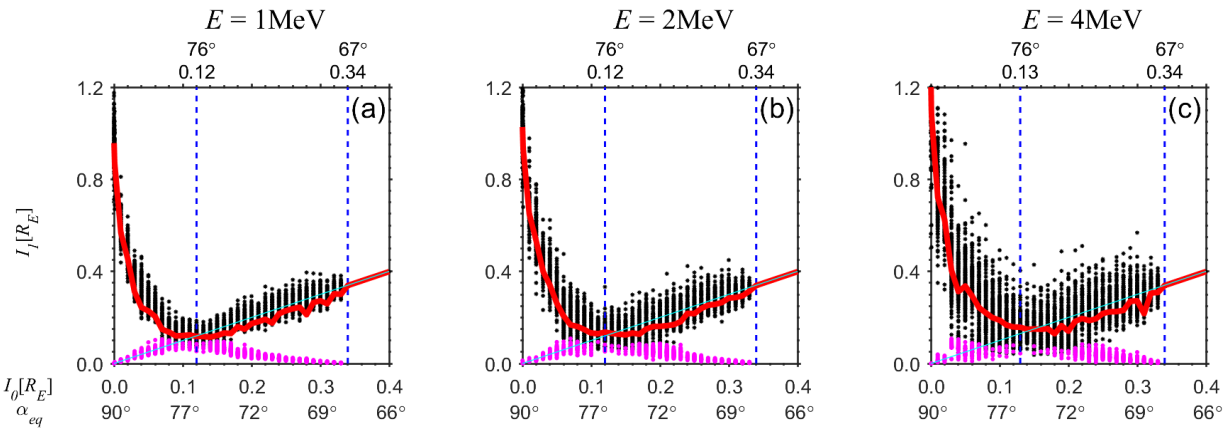

Figure 3.7: Same format as Figure 3.1b for $L_{M0} = 7.2$ and $Kp = 1$, but for electrons at $E = 1$, 2, and 4 MeV respectively in panels (a-c).

the I_0 range over which DOB occurs (up to the second blue dashed line) almost does not change with the electron energy.

3.3.3 Quantification of the Long-Term DOB Transport

After investigating the short-term DOB transport of electrons after one drift in the previous subsection, we are motivated to quantify the statistical transport of electrons due to DOB over many drift orbits. We selected three cases in Figure 3.1a for 1 MeV electrons at $L_{M0} = 6.8$, $Kp = 3$ but at different I_0 values, one in the ballistic regime (with a small I_0 of 0.0001 R_E), two in the diffusive regime (with I_0 of 0.1 and 0.4 R_E, respectively), and calculate the bounce average squared change of I, $\langle(\Delta I)^2\rangle$, over the drifts, where $\Delta I = I_k - I_0$ and I_k is the second adiabatic invariant of electrons after completing k full drifts. In the first row of Figure 3.8, we plot the values of $\langle(\Delta I)^2\rangle$ over 20 drift cycles for the three selected cases. Note that there is no drift period for the electrons on bifurcated orbits since the drift motion due to DOB is not periodic. Moreover, the time to complete one full drift cycle, unit τ_d in Figure 3.8, is different for electrons at different initial

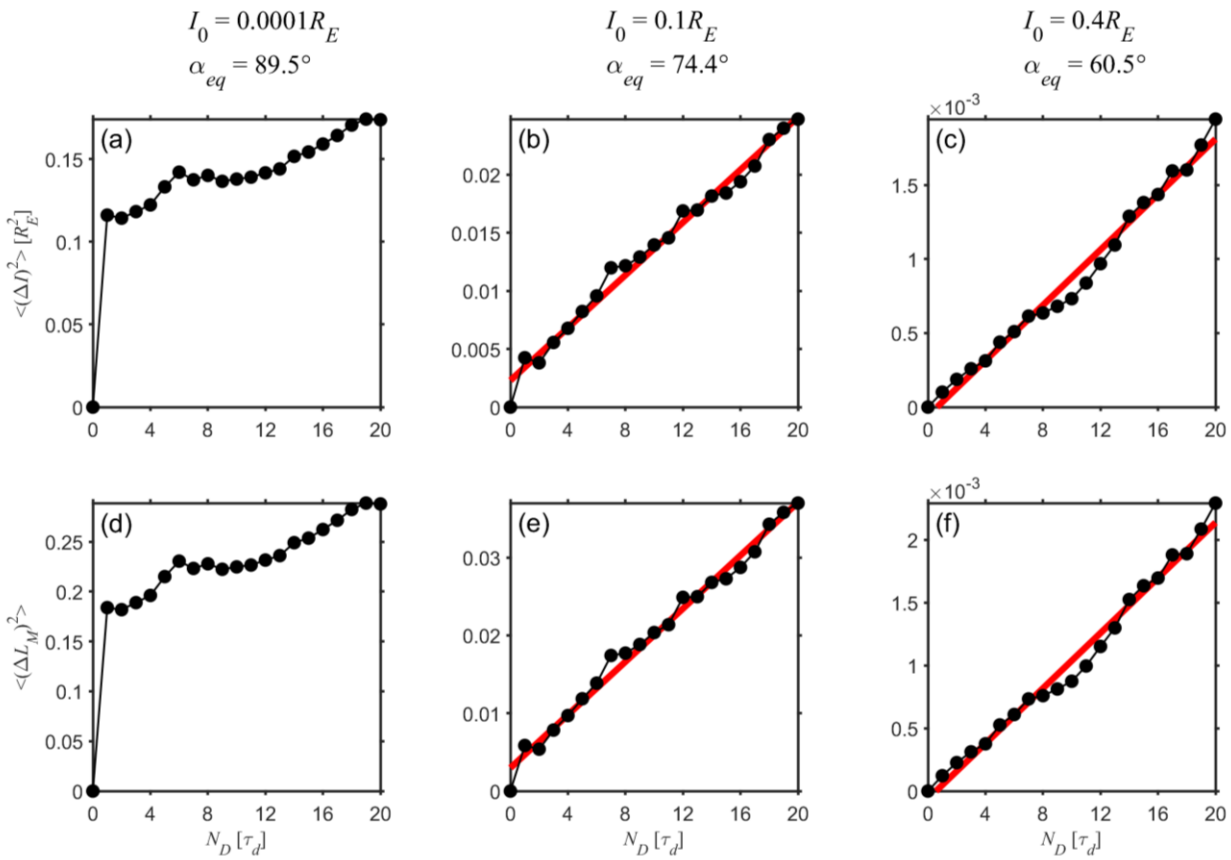

Figure 3.8: Average squared change of the second adiabatic invariant (a- c) and L_M over 20 drift cycles for 1 MeV electrons at L_{M0} = 6.8, Kp = 3 but with different initial second adiabatic invariants, 0.0001 (a, d), 0.1 (b, e), and 0.4 R_E (c, f) with corresponding equatorial pitch angle values denoted below. The red lines in (b, c, e, f) are lines of best fit.

bounce phases. Similar plots for $\langle(\Delta L_M)^2\rangle$ are shown at the bottom row, where $\Delta L_M = L_{Mk} - L_{M0}$ and L_{Mk} is the L_M value after completing k full drifts. The two diffusive cases on the right show a generally linear increase of $\langle(\Delta I)^2\rangle$ and $\langle(\Delta L_M)^2\rangle$ with time, suggesting diffusion over the long term. On the other hand, the ballistic case on the left (with I_0 = 0.0001 R_E) shows a distinctive jump in $\langle(\Delta I)^2\rangle$ and $\langle(\Delta L_M)^2\rangle$ after the first drift, which is consistent with the short-term results. The interesting feature we find is that the ballistic case also illustrates a relatively linear growth over time after the first drift, which will be investigated at the end of this section.

We focus on the diffusive cases first, based on which we could calculate the diffusion coefficients in I as $D_{II} = \langle(\Delta I)^2\rangle/(2\tau)$ and in L_M as $D_{L_M L_M} = \langle(\Delta L_M)^2\rangle/(2\tau)$, where τ is the simulation time over which the diffusion occurs and it is much longer than the drift period of electrons. Specifically, for the diffusive cases in Figure 3.8, we fit the $\langle(\Delta I)^2\rangle$ and $\langle(\Delta L_M)^2\rangle$ versus time curves with straight lines over-plotted in red, and half the slope of the fitted red line gives the value of the corresponding diffusion coefficient. This calculation of diffusion coefficients is then performed for electrons in the diffusive regime of different energies starting at different L_{M0} values and at various *Kp* levels. The results are shown in Figure 3.9 for D_{II} and Figure 3.10 for $D_{L_M L_M}$. One thing we would like to note is that there is no nontraditional DOB transport for the cases shown in Figure 3.8 for 1 MeV electrons at L_{M0} = 6.8 and *Kp* = 3, but the nontraditional DOB cases due to three *B* minima could exist in the diffusive regime, for example, magenta points in the diffusive regime of Figure 3.1b. These nontraditional DOB cases, even though non-diffusive in nature, are included in the bounce-averaging of the diffusive coefficient calculation since they are statistically insignificant, as shown in the percentage values in Figure 3.1b, and will be averaged out statistically.

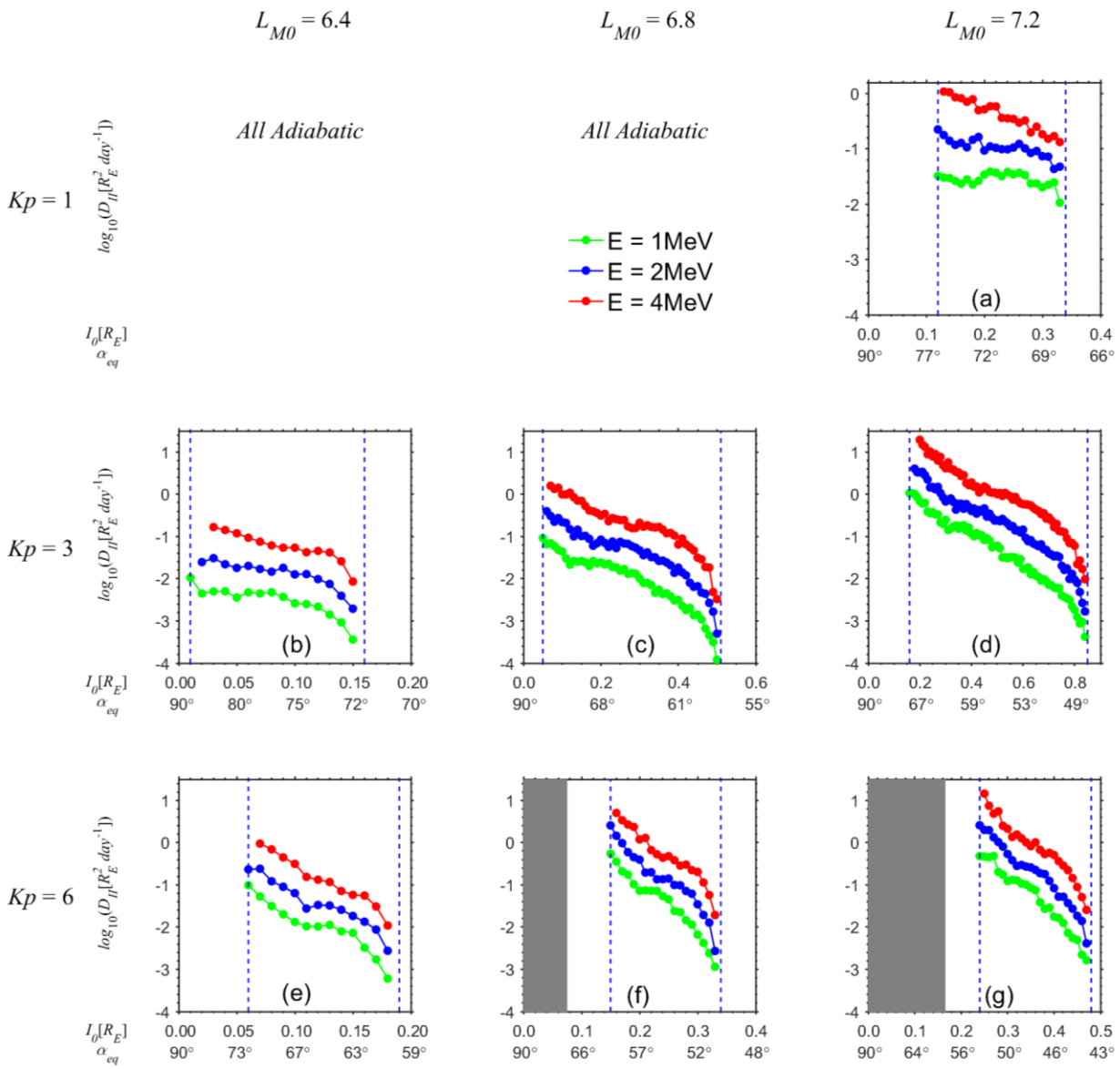

Figure 3.9: Diffusion coefficients in the second adiabatic invariant, D_{II}, due to drift orbit bifurcation at Kp = 1 (top), Kp = 3 (middle), Kp = 6 (bottom), and L_{M0} = 6.4 (left), L_{M0} = 6.8 (middle), L_{M0} = 7.2 (right), for electrons at E = 1 (green), 2 (blue), and 4 MeV (red). The x-axes are the initial second adiabatic invariant values, and the y-axis is the log value of D_{II}.

The calculated results of DOB-induced D_{II} for different electron energies are shown as curves in different colors in Figure 3.9. The blue dashed lines are the same boundary lines for the diffusive regime as in Figure 3.5 for 1 MeV electrons. Since the boundary I_0 values between the ballistic and diffusive regimes can change slightly as energy increases, the I_0 coverage of D_{II} for 2 MeV and 4 MeV electrons in blue and red may not align exactly with the blue lines. The grey areas are the same as those in Figure 3.5 for untrapped electrons. Also as in Figure 3.5, all the electrons at L_{M0} = 6.4 and 6.8 for *Kp* = 1 undergo adiabatic motions with no DOB transport. We find that at given L_{M0} and *Kp* values, the diffusion coefficient D_{II} generally decreases as the equatorial pitch angle decreases for the same electron energy level, and D_{II} is bigger for higher energy electrons at a given I_0. The energy dependence of D_{II} is consistent with the theoretical results in Öztürk and Wolf (2007) because higher energy electrons have bigger gyroradius at the mirror point and shorter drift periods. Comparing across the panels of different L_{M0} and *Kp* values, the results also show that the DOB-induced D_{II} is generally greater at larger L_{M0} and higher *Kp* levels. It is of interest to quantify the pitch angle diffusion coefficient, $D_{\alpha\alpha}$, due to DOB, and then compare the DOB-induced $D_{\alpha\alpha}$ to those caused by other pitch angle diffusion mechanisms such as scattering by chorus waves. Kim et al. (2012) showed that the bounce-averaged $D_{\alpha\alpha}$ due to chorus wave scattering is on the order of about 10^{-3} per day for 4 MeV electrons with α_{eq} = 80° at L^* = 4.5 and *Kp* = 2, which corresponds to $D_{II} \approx 10^{-3}\ R_E^2$ per day in the dipole magnetic field, which is of two orders of magnitude smaller than the D_{II} of 4 MeV electrons due to DOB at similar α_{eq} and *Kp* values even though it is at a high L_{M0} (6.4 rather than 4.5) as shown in the red dots of Figure 3.9b.

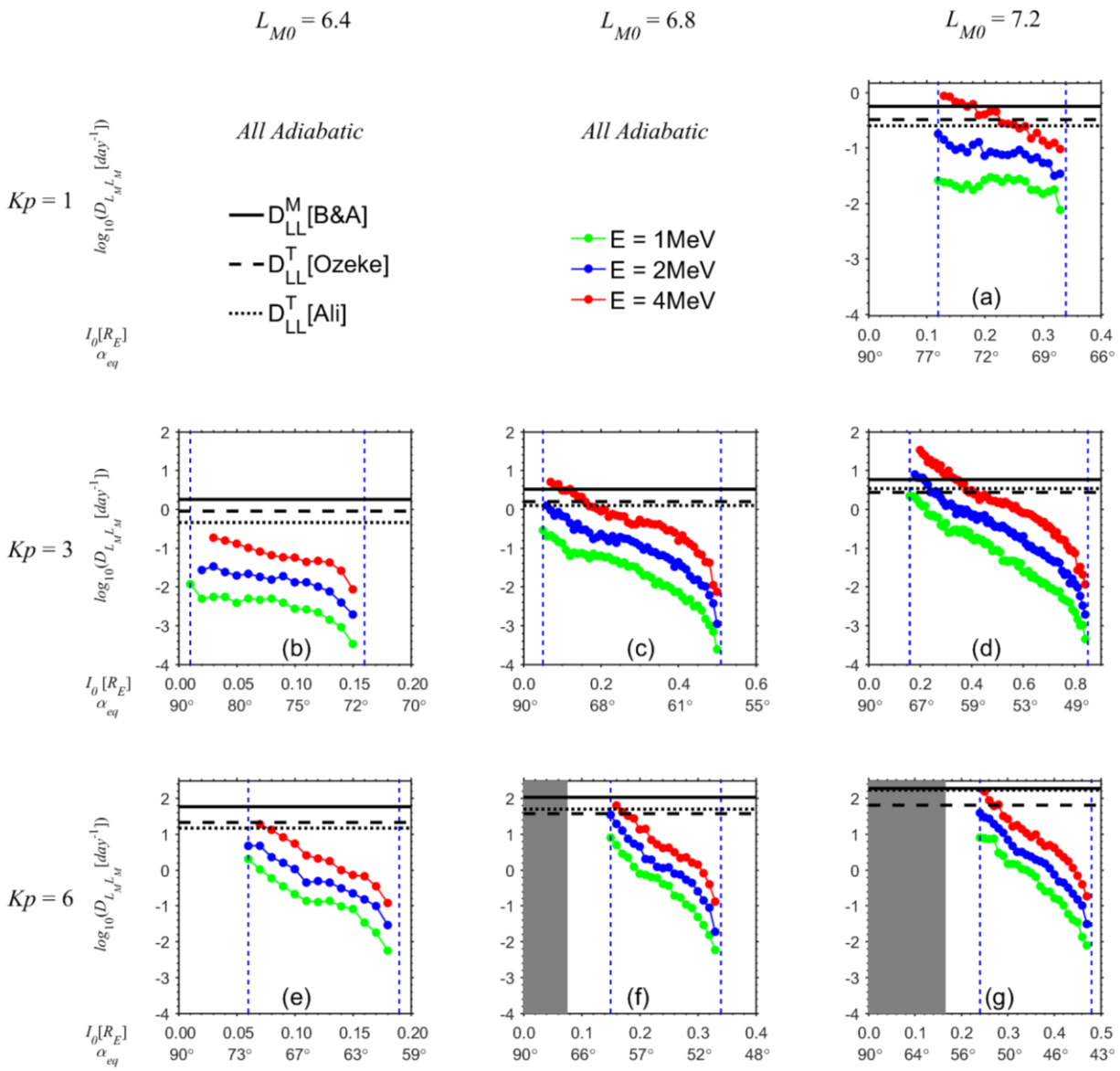

Figure 3.10: Same format as Figure 3.9, but for the diffusion coefficient of the L_M due to drift orbit bifurcation with the y-axis being the log value of $D_{L_M L_M}$. The solid, dashed, and dotted black lines are D^M_{LL}[B&A], D^T_{LL}[Ozeke], and D^T_{LL}[Ali], respectively.

The calculated $D_{L_M L_M}$ due to DOB transport, shown in Figure 3.10, show similar dependence on L_{M0}, *Kp*, electron energy, and equatorial pitch angle as D_{II}, that is, higher $D_{L_M L_M}$ at higher electron equatorial pitch angles and energies, and at higher L_{M0} and *Kp*. To investigate the significance of DOB effects, it is helpful to compare the DOB-induced $D_{L_M L_M}$ with the electron radial diffusion coefficients caused by drift-resonance with ULF waves, even though L_M may not be the same as the L parameters used in various ULF-wave-driven D_{LL} models (ranging from dipole L, McIlwain L (McIlwain, 1961), to L^* (Roederer & Zhang, 2014)). For example, the Brautigam and Albert (2000) magnetic radial diffusion coefficients,

$$D_{LL}^{M}[\text{B\&A}] = 10^{(0.506Kp - 9.325)} L^{10} \text{ [day}^{-1}\text{]}, \; Kp = 1 \text{ to } 6, \tag{3.2}$$

at different L (applied using the same value as L_M) and *Kp* values are plotted as solid black lines in Figure 3.10. The sum of the magnetic and electric radial diffusion coefficient $D_{LL}^{T}[\text{Ozeke}]$ from Ozeke et al. (2014),

$$D_{LL}^{B} = 6.62 \times 10^{-13} L^{8} 10^{-0.0327L^2 + 0.625L - 0.0108Kp^2 + 0.499Kp} \text{ [day}^{-1}\text{]}, \tag{3.3}$$

$$D_{LL}^{E} = 2.16 \times 10^{-8} L^{6} 10^{0.217L + 0.461Kp} \text{ [day}^{-1}\text{]}, \tag{3.4}$$

$$D_{LL}^{T}[\text{Ozeke}] = D_{LL}^{B} + D_{LL}^{E} \text{ [day}^{-1}\text{]}. \tag{3.5}$$

are plotted as dashed black lines. The dotted black lines are the sum of the magnetic and electric radial diffusion coefficients $D_{LL}^{T}[\text{Ali}]$ from Ali et al. (2016),

$$D_{LL}^{B}[\text{RBSP}] = \exp\left(a_1 + b_1 \cdot Kp \cdot L^* + L^*\right) \text{ [day}^{-1}\text{]}, \tag{3.6}$$

$$D_{LL}^{E}[\text{RBSP}] = \exp\left(a_2 + b_2 \cdot Kp \cdot L^* + c_2 \cdot L^*\right) \text{ [day}^{-1}\text{]}, \tag{3.7}$$

$$D_{LL}^{T}[\text{Ali}] = D_{LL}^{B}[\text{RBSP}] + D_{LL}^{E}[\text{RBSP}] \text{ [day}^{-1}\text{]}, \tag{3.8}$$

where the constants are

$$a_1 = -16.253, \; b_1 = 0.224,$$

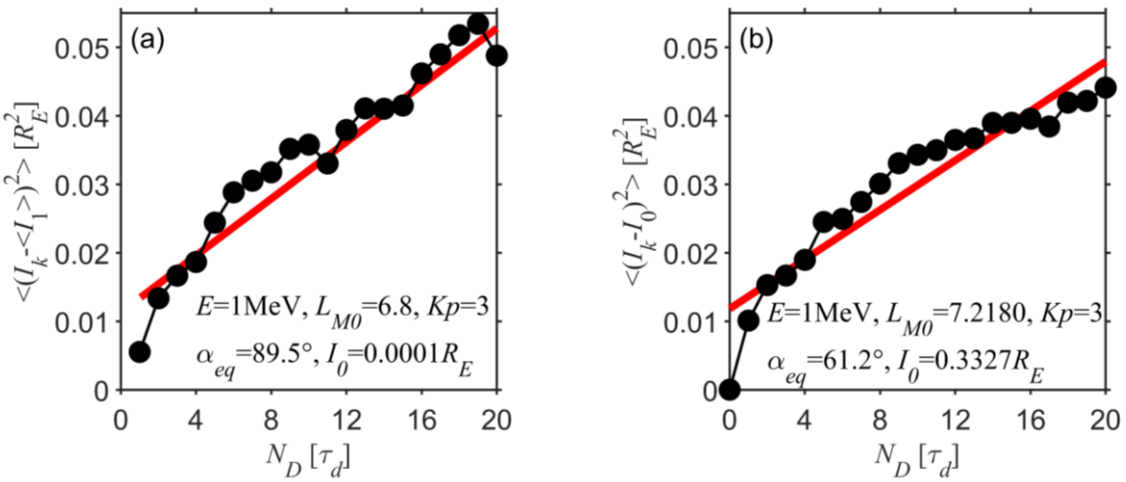

Figure 3.11: Same format as Figure 3.8, but the y-axis in panel (a) shows the values of $\langle (I_k - \langle I_1 \rangle)^2 \rangle$ after the first drift cycle.

$$a_2 = -16.951,\ b_2 = 0.181,\ c_2 = 1.982.$$

All three empirical models of ULF-wave-driven D_{LL} are shown as single horizontal lines in each panel since they have no energy or pitch angle dependence. By comparing the DOB-driven $D_{L_ML_M}$ with the ULF wave-driven D_{LL}, we see that $D_{L_ML_M}$ could become comparable to the ULF wave-driven D_{LL} at high equatorial pitch angles, and can be even greater than the ULF wave-driven D_{LL} for higher energy electrons at larger L_{M0}, suggesting that DOB could play a significant role in the radial transport of radiation belt electrons.

Quantifying the long-term transport of electrons in the ballistic regime is more challenging than those in the diffusive regime. Based on the short-term transport results in Figures 3.5 and 3.6, electrons in the ballistic regime under traditional DOB transport generally jump to a larger I_1 (and L_{M1}) value after the first drift cycle. Then this larger I_1 value (practically the new I_0 value for the second drift) could fall into the diffusive regime and lead to diffusive DOB transport afterward. Then to simulate the long-term transport of electrons in the ballistic regime, it may be adequate to specify the jumps in I and L_M from the first drift orbit and then use the diffusive coefficients

derived for the diffusive cases discussed above for subsequent transport. To validate this hypothesis, we examine a ballistic case shown in Figures 3.8a and 3.8d for 1 MeV electrons at L_{M0} = 6.8, Kp = 3 with I_0 = 0.0001. Based on the bounce phase averaged red curves in Figures 3.5e and 3.6e, after the first drift cycle these electrons will jump to averaged values of $\langle I_1 \rangle \sim 0.3327\ R_E$ and $\langle L_{M1} \rangle \sim 7.2180$, which fall into the diffusive regime according to the simulation results shown in Figures 3.5f and 3.6f. Then instead of plotting $\langle (\Delta I)^2 \rangle = \langle (I_k - I_0)^2 \rangle$ over all the drifts as in Figure 3.8, we calculate and plot $\langle (I_k - \langle I_1 \rangle)^2 \rangle$ over time from after the first drift, as shown in Figure 3.11a. The curve illustrates a generally linear growth over time, which supports our hypothesis. For a more quantitative comparison, in Figure 3.11b we plot $\langle (\Delta I)^2 \rangle = \langle (I_k - I_0)^2 \rangle$ for 1 MeV electrons directly starting from the $I_0 \sim 0.3327\ R_E$ and $L_{M0} \sim 7.2180$ at Kp = 3 and find that the $\langle (\Delta I)^2 \rangle$ transport is very similar to that of Figure 3.11a. The slight difference is due to the fact that the jump in I and L_M after the first drift can be bounce phase dependent, as shown in the vertical spread in Figures 3.5 and 3.6; using the averaged values of $\langle I_1 \rangle$ and $\langle L_{M1} \rangle$ to represent the electron state in I and L_M after the first drift cycle is only approximate and can lead to uncertainties. Nevertheless, our results suggest that the long-term transport of electrons in the ballistic regime could be a combination of advection and diffusion where the electrons undergo a ballistic jump in I and L_M within the first drift and then illustrate diffusive transport afterward.

3.4 Conclusions and Discussion

The traditional DOB happens when the dayside magnetosphere is compressed by the solar wind, exhibiting two local magnetic field minima on either side of the equator, that is, a W-shaped field line. When particles traverse the dayside compressed region, they could be temporarily trapped in one of the hemispheres off the equator when the magnetic field strength at the local

maximum at the equator exceeds the magnetic field strength at the particle's mirror points (B_m). The first adiabatic invariant and B_m are constant during DOB, but the second adiabatic invariant I is violated, leading to particle transport in both I and radial distance due to the constant B_m. To better quantify the transport of energetic electrons due to the DOB effects, we use a guiding center test particle code to model the short-term and long-term transport of electrons in I and L_M (equatorial radial distance at midnight) in the T89c magnetic field model under different electron and geomagnetic conditions.

The short-term simulation results after one drift show both traditional DOB transport, in which electrons undergo ballistic jumps at large equatorial pitch angles or small I_0 (defined as the ballistic regime), and diffusive transport at bigger I_0 (defined as the diffusive regime), as well as nontraditional DOB transport, in which electrons show diffusive transport in the traditionally defined ballistic regime and ballistic jumps in the traditional diffusive regime. Even though our results show that the nontraditional DOB effects could have a minor effect on the statistically averaged transport of electrons, their distinct transport on electrons is still interesting and is reported here for the first time. Furthermore, we find that the nontraditional DOB cases are caused by three local B minima along the magnetic field line rather than two local B minima for the traditional DOB cases, and their effects are more significant at larger L_{M0} and smaller I_0 values. By further investigating the L_M, Kp, and E dependence of the short-term DOB transport, we find that the DOB effects are more significant at larger L_{M0}, higher Kp, and for electrons of higher energies. The results suggest that DOB can penetrate inside the geosynchronous orbit at $Kp \geqslant 3$, and the jump in L_M due to DOB can be quite significant for high equatorial pitch angle electrons, for example, with $\langle \Delta L_M \rangle$ reaching 4 R_E at $Kp = 6$ and $L_{M0} = 6.4$. These demonstrate that DOB can play a significant role in the electron transport in the outer radiation belt.

In addition, the long-term DOB transport of electrons is investigated based on our simulation results over many electron drifts. For electrons in the diffusive regime, the diffusion coefficients in I as D_{II} and in L_M as $D_{L_ML_M}$ are calculated, which show higher D_{II} and $D_{L_ML_M}$ at higher electron equatorial pitch angles and energies and at larger L_{M0} and Kp values. Moreover, we find the DOB-induced D_{II} could be two orders of magnitude higher than the bounce-averaged D_{II} due to pitch angle diffusion by chorus waves. Please note that the pitch angle diffusion by DOB is drift averaged since it is occurring over the time scale of drifts, while the chorus-induced pitch angle diffusion is bounce averaged. In addition, the DOB-induced $D_{L_ML_M}$ could be comparable to or even higher than the D_{LL} driven by ULF waves at high electron equatorial pitch angles. This suggests that DOB could lead to significant transport of energetic electrons even in the absence of waves, contributing to the fast dropout of radiation belt electrons. Furthermore, the long-term simulation results for electrons in the ballistic regime show that their transport could be approximated as a combination of advection and diffusion where the electrons undergo ballistic jump in I and L_M after the first drift and then diffusive transport afterward. This was suggested in Ukhorskiy et al. (2011) but demonstrated more quantitatively here. Further validation of this approximation requires detailed comparisons between our test particle simulation results and the simulation results from, for example, an advection-diffusion model driven by DOB transport rates quantified from the test particle results. The long-term electron transport due to DOB quantified in this work is found to be generally consistent with that from some of the previous works. For example, our results in Figure 3.8d show that $\langle(\Delta L_M)^2\rangle^{1/2}$ is around 0.5 after 10 drift cycles, which is similar to the result in Figure 3.9a of Ukhorskiy et al. (2011) with $0.5 < \langle(\Delta L_M)^2\rangle^{1/2} < 1.0$ for small I_0 ($< 0.1\ R_E$) at $L_{M0} = 6.8$ after 10 drift cycles in the TS07D model with solar wind dynamic pressure $P_{dyn} = 3$ nPa. However, the transport quantification present in this work is more

comprehensive covering various *L* values, energies, and equatorial pitch angles at different geomagnetic conditions. Overall, the long-term transport rates of electrons due to DOB quantified in this work are very useful, which could be applied to global radiation belt modeling for studying the relative importance of DOB to the loss and transport of radiation belt electrons.

Finally, we will discuss some potential limitations in our simulation results and the quantified DOB transport. First, for the test particle simulations, we have chosen the T89c magnetic field model since it is solely controlled by the *Kp* index, which makes it easier to parameterize the quantified DOB transport rate of electrons as a function of electron and geomagnetic conditions in the future for applications in global radiation belt modeling. However, we are aware that the T89c model may not be as realistic as other magnetic field models, such as the TS04 field model, especially during storm time (Tsyganenko & Sitnov, 2005). But those models are driven by a group of solar wind and geomagnetic parameters and are usually more computationally expensive. Thus, they are more suitable for simulating DOB effects during individual events. In addition, the three local *B* minima features that lead to nontraditional DOB transport in our simulation results can be magnetic field model dependent. For the T89c model, by testing the contribution from various current systems in the model we find that the three *B* minima is mainly contributed by the ring current system in T89c. However, in the TS04 field model the three *B* minima region is found to be generally located near the magnetopause boundary right before the open field line region, rather than between the single local *B* minimum and two local *B* minima regions, as shown in Figure 3.3 for the T89c model. The three B minima region found in the TS04 field model is also consistent with the three *B* minima region found near the magnetopause in the global MHD fields in Desai et al. (2021). In this case, the effects of the nontraditional DOB transport can be less significant since the three *B* minima region is further out.

Nevertheless, detailed event studies are still needed to investigate the significance of nontraditional DOB cases in these other field models in the future.

Second, since L^* is not defined on bifurcated drift orbits, for long-term radial transport of electrons, we have used the L_M parameter and quantified the diffusion coefficient using $D_{L_M L_M}$, which is similar to the approach in Ukhorskiy et al. (2011). Since the global radiation belt models are in adiabatic invariant space (e.g., Tu et al., 2013; Tu et al., 2014b), to obtain a parameter close to the Roederer L^*, Ukhorskiy et al. (2014) calculated a generalized $\bar{L}$ parameter by integrating the magnetic flux over the unclosed drift shells caused by DOB. This $\bar{L}$ parameter, though more computationally expensive to calculate, could be more physical when implementing the parameterized radial diffusion coefficient of electrons due to DOB into global radiation belt models.

Lastly, other processes in static magnetic fields, such as field line curvature (FLC) scattering in the stretched magnetotail and current sheet scattering in the magnetopause, could violate the first adiabatic invariant of electrons and the guiding-center approximation. FLC scattering happens when the gyroradius of the particle is comparable to the radius of curvature of the field line. Unlike DOB, FLC scattering violates the first adiabatic invariant of electrons, leading to electron transport in pitch angle (e.g., Tu et al., 2014a; Yu et al., 2020) and current sheet scattering may occur when electrons reach the magnetopause for which the finite gyroradius effects are important (e.g., Mauk et al., 2016). Since we focus on the DOB effects in this work, a guiding-center test particle code is justified. However, it is important to recognize that these other processes can occur simultaneously with DOB and lead to additional electron transport in pitch angle.

Chapter 4

Modeling the Effects of Drift Orbit Bifurcation on the Magnetopause Shadowing Loss of Radiation Belt Electrons: Data-Model Comparisons

This chapter is based on the paper in preparation for Geophysical Research Letters, Modeling the Effects of Drift Orbit Bifurcation on the Magnetopause Shadowing Loss of Radiation Belt Electrons by Jinbei Huang, Xingzhi Lyu, Weichao Tu, Jay M. Albert, and Sang-Yun Lee.

4.1 Introduction

As mentioned in Section 2.4.3, LCDS has been widely used for studying the magnetopause shadowing loss. However, Drift Orbit Bifurcation (DOB), which is a process that may lead to the change of the second adiabatic invariant K, should be carefully considered in the estimation of LCDS (George et al., 2022; Olifer et al., 2018, 2021; Tu et al., 2014b, 2019; Xiang et al., 2017; Yu et al., 2013). DOB occurs when the dayside magnetosphere is compressed by the solar wind, resulting in a W-shaped magnetic field strength profile with two minima off the magnetic equator and a maximum at the equator. When a particle bounces between two hemispheres, it can become trapped on one side of the hemisphere if it crosses the W-shaped field strength region, known as the bifurcation region, if its B_m (the magnetic field intensity at the particle's mirror points) is smaller than the equatorial magnetic field maximum (Huang et al., 2022; Öztürk & Wolf, 2007; Ukhorskiy et al., 2011). DOB violates both the 2nd and 3rd adiabatic invariants of electrons, and the L^* becomes undefined. Therefore, the traditional method of obtaining LCDS by tracing magnetic field lines with constant second invariant cannot physically include DOB. To test the DOB effects in the LCDS calculation, Albert et al. (2018) utilized a guiding center test particle code to compute the LCDS through two approaches to addressing DOB: rejecting DOB and including DOB. The

former approach assumes that electrons with a bifurcated drift shell are all lost within one drift, which could lead to an overestimation of the electron loss since results show that electrons can remain trapped in the radiation belt after the transport due to DOB (e.g., Huang et al., 2022). In the latter approach of including DOB, the test particle code continues to trace the full drift trajectory of electrons after bifurcation and a pseudo-L^* is calculated based on the magnetic flux enclosed by the drift shell (even though it is not closed). Then Albert et al. (2018) compared the LCDS calculated from these two approaches with the LCDS calculated using the traditional approach by tracing field lines with constant second invariant, and suggested that that the LCDS calculated by these three different approaches can be very different during geomagnetic storms.

Even though previous work has shown that DOB can have significant effects on the LCDS of radiation belt electrons, its effects on the dropout of radiation belt electrons have not been quantified. In this study, for the first time, we implement the event-specific LCDS calculated using three different approaches to dealing with DOB, i.e., tracing field lines ignoring DOB, tracing test particles rejecting DOB, and tracing test particles including DOB, into a radial diffusion model, to quantify the DOB effects on the observed magnetopause shadowing loss of radiation belt electrons during the May 2017 dropout event.

4.2 Event Analysis

The event we selected for this study is during May 27-28, 2017, when an intense geomagnetic storm occurs with SYM-H reaching ~-150 nT as shown in Figure 4.1e. The solar wind dynamic pressure P_{dyn} and the interplanetary magnetic field B_z during the event are plotted in Figure 4.1d in black and blue, respectively. Figure 4.1a-4.1b plot the Phase Space Density (PSD)

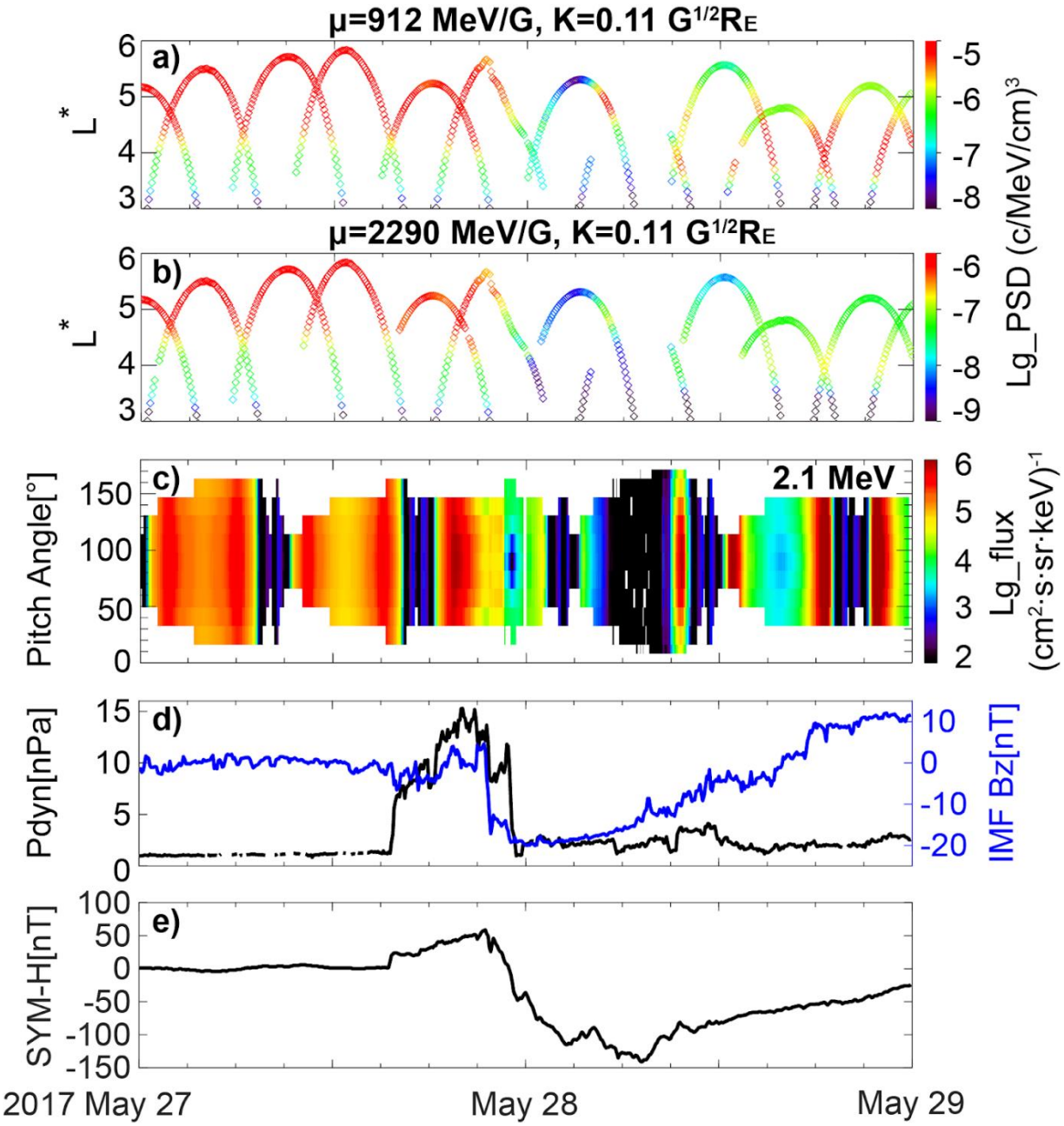

Figure 4.1: Phase Space Density (PSD) of (a) μ = 912 MeV/G, (b) μ = 2290 MeV/G, and K = 0.11 $G^{1/2}R_E$ electrons as a function of time and L^*. (c) 2.1 MeV electron fluxes versus local pitch angle and time observed by Van Allen Probe A along its orbit. (d) Solar wind dynamic pressure in the black line, IMF B_z in blue, and (e) SYM-H index during May 27-28, 2017.

of the electrons with first adiabatic invariant μ = 912 MeV/G and K = 0.11 $G^{1/2}R_E$ (corresponding to ~2.2 MeV electrons at L ~ 5), μ = 2290 MeV/G and K = 0.11 $G^{1/2}R_E$ (corresponding to ~5.5 MeV electrons at L ~ 5) as a function of time and L^*, respectively. The PSD is calculated based on the flux data measured by the Relativistic Electron Proton Telescope (REPT) (Baker et al., 2013) and the Magnetic Electron Ion Spectrometer (MagEIS) instruments (Blake et al., 2013) onboard Van Allen Probes, using the TS04 magnetic model (Tsyganenko & Sitnov, 2005). Fast electron dropout in PSD is observed at high L^* around 03 UT of May 28 for a wide range of μ values, which indicates loss of electrons through magnetopause shadowing. Figure 4.1c illustrates the 2.1 MeV electron fluxes as a function of local pitch angle and time, observed by Van Allen Probe A along its orbit. The observed fluxes at approximately 23 UT of May 27 near the apogee exbibit a distinct butterfly pitch angle distribution (PAD), which is a typical PAD feature of the magnetopause shadowing loss due to the drift shell splitting effect (Roederer & Zhang, 2014; Tu et al., 2019). The observed loss features discussed above suggest that magnetopause shadowing loss could be the dominant loss mechanism contributing to the dropout of outer radiation belt electrons during the geomagnetic storm on 27 May 2017, especially at high L^* regions.

4.3 Simulation and Results

4.3.1 Radial Diffusion Simulation

To simulate the magnetopause shadowing loss associated with the outward radial diffusion of electrons during the May 2017 electrons dropout event, we employ a one-dimensional radial diffusion model that solves the simplified Fokker-Planck equation (Schulz & Lanzerotti, 1974):

$$\frac{\partial f}{\partial t} = L^{*2}\frac{\partial}{\partial L^*}\left(\frac{D_{LL}}{L^{*2}}\frac{\partial f}{\partial L^*}\right) - \frac{f}{\tau}. \tag{4.1}$$

Here, f represents the electron PSD at a fixed μ and K. D_{LL} denotes the radial diffusion coefficient, and τ stands for the electron e-folding lifetime, which refers to the time it takes for a quantity to decrease by a factor of "e", where "e" is the base of the natural logarithm. The D_{LL} is obtained from the empirical magnetic radial diffusion coefficient proposed by Brautigam and Albert (2000). To represent the magnetopause shadowing loss, electron lifetimes outside the LCDS are assumed to be on the order of electron drift periods, which vary with energy and pitch angle (Schulz & Lanzerotti, 1974). The model outer boundary is defined at L^* = 11 with Neumann boundary condition ($\partial f/\partial L$ = 0), and L^* = 11 is always outside the LCDS during this event. In our simulations, the Crank-Nicolson algorithm is used to solve the above Fokker-Planck equation numerically.

The event-specific LCDS used in our model is calculated using the TS04 magnetic field model by implementing the three different approaches to dealing with the DOB effects following Albert et al. (2018) (discussed in Section 4.1). The results are shown in Figure 4.2 panel (a1) for K = 0.05 $G^{1/2}R_E$. The first approach is the traditional approach by tracing magnetic field lines with constant second invariant using the LANLGeoMag library (Henderson et al., 2018). The calculated LCDS is depicted as the green line in panel (a1) and labeled as LCDS(TF), which is shown to drop to as low as L^*=4 during the storm main phase. The approach is not physical when DOB occurs since the second invariant is violated in DOB. The second and third approaches are based on the guiding center test particle code that solves the guiding center equations proposed by Brizard and Chan (1999):

$$\begin{cases} \dfrac{d\vec{R}}{dt} = \dfrac{p_{\parallel}}{\gamma m}\dfrac{\vec{B}^*}{B_{\parallel}^*} + \dfrac{\mu}{\gamma q}\dfrac{\hat{b}\times\nabla B}{B_{\parallel}^*}, \\ \dfrac{dp_{\parallel}}{dt} = -\dfrac{\mu}{\gamma}\dfrac{\vec{B}^*\cdot\nabla B}{B_{\parallel}^*}, \end{cases} \tag{4.2}$$

where $\vec{B}^* = \vec{B} + (p_{\parallel}/q)\nabla\times\hat{b}$, $\hat{b}$ is the unit vector of $\vec{B}$, $\vec{R}$ is the electron guiding center position, $p_{\parallel}$ is the parallel momentum of the electron, γ is the Lorentz factor, m and q are the mass and charge of the electron, and μ is the first adiabatic invariant. The fourth-order Runge-Kutta method is used to solve the guiding center equations numerically. In the test particle approaches, we launch electrons in the TS04 model from the magnetic equator at MLT = 3 with different K values to find the LCDS as a function of K. In the second approach, tracing test particles while rejecting DOB, electrons with a bifurcated drift shell are assumed to be lost within one drift (thus on open drift shells). This approach could be "overkill" since electrons suffering from DOB may still be trapped in the radiation belt. The LCDS resulting from this approach is represented by the orange line in Figure 4.2a1 and labeled as LCDS(TPR). While in the third approach, tracing test particles while including DOB, the magnetic flux enclosed by the bifurcated drift shells are still calculated using the foot points of the field lines mapped to the Earth's surface (Albert et al., 2018; Ukhorskiy et al., 2014), which generates a pseudo-L^* in the presence of DOB. This approach could more physically include the DOB effects than the second approach. The LCDS obtained using this approach is represented by the purple line in Figure 4.2a1 and labeled as LCDS(TPI).

Comparing the LCDS values obtained using the three different approaches in panel (a1), we find that they all decrease during the storm main phase. Before 23UT of May 27 and after 16UT of May 28 of the storm, the tracing test particles including DOB (TPI) approach generally yields

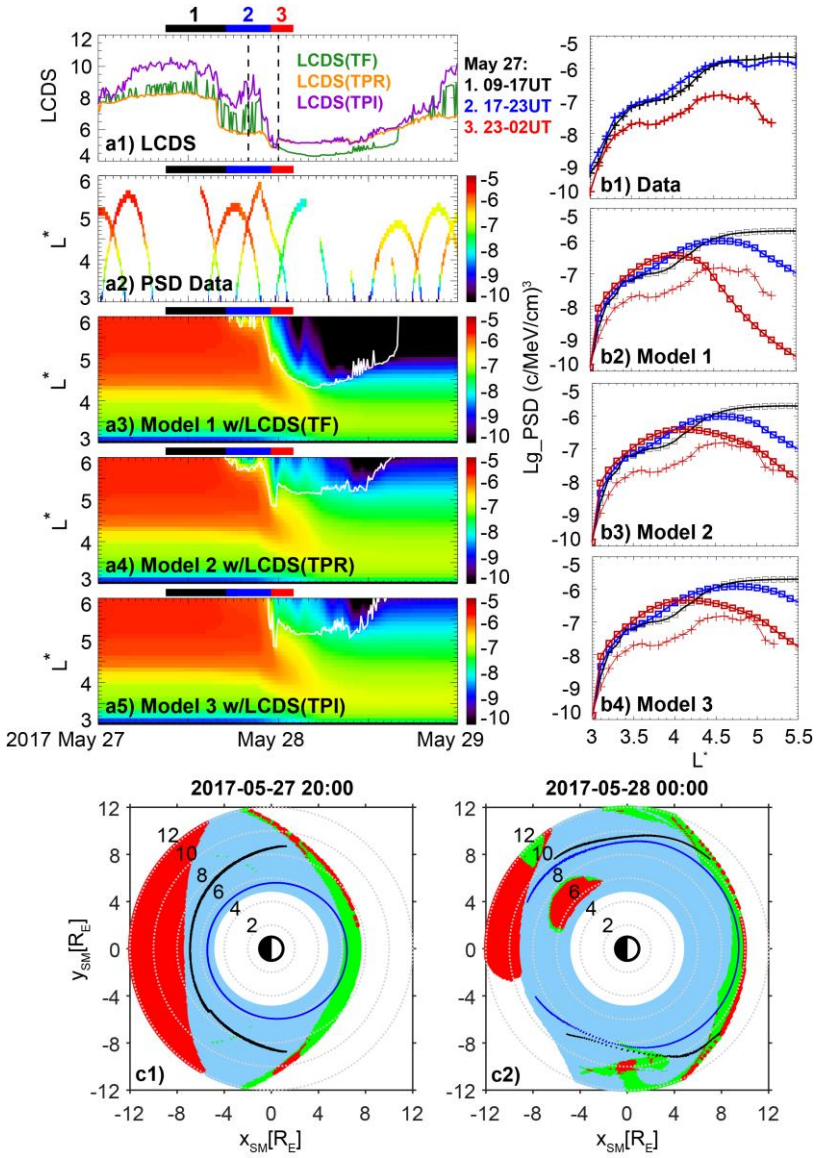

Figure 4.2: (a1) Different Last Closed Drift Shell (LCDS) results with Trace Field lines (TF) in green, Trace Particles Reject DOB (TPR) in orange, and Trace Particles Including DOB (TPI) in purple, of K = 0.05 $G^{1/2}R_E$ electrons as a function of time. (a2-a5) Electron PSD data and simulation results for μ = 2290 MeV/G, and K = 0.05 $G^{1/2}R_E$, with the white curves in (a3-a5) representing the LCDS locations calculated by different approaches. (b1-b4) Observed and simulated PSD versus L^* profiles from panels (a2-a5) averaged over three different time intervals, where (b2-b4) correspond to the model results in (a3-a5), respectively. The thin red lines in (b2-b4) with "+" symbols are copied from the data shown in panel (b1). (c1-c2) Blue and black curves: equatorial crossings of the electrons' trajectories from the test particle simulation for the LCDS from the Trace Particles Rejecting DOB approach in blue, and Trace Particles Including DOB approach in black. The colors in the region with radial distances of 5-12 R_E represent the number of local magnetic field minima along the field lines: blue for one, green for two, red for at least three, and white region for open field lines. (c1) and (c2) are plotted for the two times marked by the two dashed vertical lines in (a1).

the largest LCDS value, rejecting DOB (TPR) yields the smallest LCDS, and tracing field lines (TF) falls in between. These findings are consistent with the results reported by Albert et al. (2018). We think the bumpy feature of the LCDS by tracing field lines (TF) arises from the unphysical treatment of DOB in this approach by tracing a constant second adiabatic invariant. This LCDS difference between the two test particle approaches could be understood using Figure 4.2 panel (c1) in which the colors in the region with a radial distance of 5-12 R_E from Earth represent the number of local magnetic field minima along the local field line, with blue for one minimum, green for two minima, and red for at least three minima, respectively, while white color represents open field lines. We can see that the open field lines cover a wide region on the dayside due to the high solar wind P_{dyn} at this time. In addition, the high P_{dyn} compresses the dayside magnetosphere and leads to an increased local magnetic maximum at equator, which is favorable for DOB to occur. Consequently, a wide bifurcation region with two local magnetic field minima (green area) appears on the dayside, which leads to considerable differences between LCDS values by including DOB vs. rejecting DOB as shown in panel (a1) at this time (marked by the first dashed vertical line). These two LCDS are also plotted in panel (c1) with the LCDS(TPR) (rejecting DOB) as the blue curve and LCDS(TPI) (including DOB) as the black curve. Specifically, these curves illustrate the equatorial crossings of the test electrons' trajectories at the LCDS. The gap in the black curve on the dayside is due to the bifurcated drift shells not crossing the equator. We can see that the LCDS by rejecting DOB is located a lot closer to Earth than the LCDS by including DOB, corresponding to the large difference between them.

However, during the period from 23UT of May 27 to 16UT of May 28, we see that the difference between the test-particle LCDS with rejecting DOB (TPR) and including DOB (TPI) becomes much smaller and the LCDS by tracing field lines (TF) stays much lower than the LCDS

by tracing test particles. To understand this, we create a similar magnetic configuration plot for the time of 00UT of May 28 in panel (c2). There are less open field line regions (in white) on the dayside due to the lower solar wind P_{dyn}. As a consequence, the bifurcation region (in green) is also narrower on the dayside, leading to smaller difference between the LCDS by rejecting DOB (the blue curve) and by including DOB (the black curve). The gaps in the two curves on the nightside are a result of the stretched asymmetric magnetic field lines with a complicated configuration. Furthermore, the lower LCDS from the tracing field line approach during this interval is due to the local magnetic field anomalies illustrated by the small red blob (with at least three local magnetic field minima) in the post-dusk region between 6-8 R_E, which could possibly be related to the presence of a partial ring current on the nightside (Tsyganenko et al., 2021) but its physical cause and validity still remains to be explored. These field anomalies could lead to unphysical open trajectories of electrons in between physical and closed drift shells of electrons. In our approaches of calculating LCDS by tracing test particles, we are able to jump over this region and achieve the more physical LCDS values. However, the LANLGeoMag library we used in the tracing field line approach doesn't currently have a mechanism to jump over this region when searching for the LCDS, thus leading to lower LCDS values than those with the tracing test particle approaches.

4.3.2 Simulation Results in PSD

With the LCDS calculated by the three different approaches described above, we then implemented them into the radial diffusion model to quantify their effects on reproducing the observed losses of radiation belt electrons. Figure 4.2 panels (a3-a5) present the simulation results for the same μ and K values as the PSD data in panel (a2), with μ = 2290 MeV/G, and K = 0.05

$G^{1/2}R_E$, and with the white curves representing the LCDS values obtained from the three different methods shown in panel (a1). Model 1 is with LCDS(TF), Model 2 is with LCDS(TPR), and Model 3 is with LCDS(TPI). We find that the models with different LCDS could all generate fast magnetopause shadowing loss of electrons at higher L^*, owing to the low LCDS values during the storm main phase from all three approaches. To conduct a detailed comparison with data and examine the differences in results among the three approaches of LCDS calculation, we select three consecutive time intervals during the event to investigate the detailed evolution of PSD versus L^* profiles. The time coverage for each interval is represented by a horizontal color bar at the top of panels (a1-a5), with the UT hours indicated on the right side of panel (a1). Panels (b1-b4) exhibit the comparison between the data (panel (b1)) and model results (panels (b2-b4)) in the evolution of PSD versus L^* profiles. The profiles for intervals #1, #2, and #3 are represented by the black, blue, and red curves, respectively. During interval #1, the pre-storm phase, both data and model exhibit similar profiles with positive PSD versus L^* gradient. During interval #2, the initial phase of the storm, LCDS(TPI) stays higher than LCDS(TPR) and LCDS(TF) (see panel (a1) or the white curves in panels (a3-a5)), and at the end of interval #2, LCDS(TF) in Model 1 and LCDS(TPR) in Model 2 both drops to $L^* = 4.9$, while LCDS (TPI) in Model 3 only drops to $L^* = 5.3$. By comparing the PSD vs. L^* profiles during interval #2, we find that the data only show a small drop at large L^* which is overestimated by Model 1 and Model 2. This overestimation is improved in Model 3 with higher LCDS values during this interval, which demonstrates that physically including DOB in the LCDS calculation best reproduces the observed loss of electrons. Finally, during interval #3 in the storm main phase, the LCDS was first pushed to as low as $L^* = 4.9$ for Model 1, $L^* = 4.8$ for Model 2 and Model 3, and then recovered to $L^* = 5.3$ for Model 2 and Mode 3 towards the end of the interval. For Model 1, the LCDS initially recovers to $L^* = 5.1$

shortly after the beginning of the interval, but then drops to $L^* = 4.5$ by the end of the interval due to the inability of the tracing fields method to handle the field anomalies as discussed in section 4.3.1. The lower LCDS values in Model 1 leads to an overestimation of electron loss at high L^* (thick red curves in panel (b2), with the thin red curve marked by "+" symbols copied from the data plot in panel (b1)). However, the losses produced during interval #3 by Model 2 and Model 3 (thick red curves in panels (b3) and(b4)) well captures the observed electron dropout at high L^* regions (compared to thin red curves copied from the data plot). Furthermore, all the three models (panels (b2-b4)) exhibit fast loss at large L^* and an internal PSD peak at low L^*, which are typical magnetopause shadowing loss features in which the shadowing first eliminates electrons outside the low LCDS, and as the LCDS relaxes to larger L^*, the electrons diffuse both inward and outward creating an internal PSD peak (Shprits et al, 2006; Turner et al., 2012). One thing we notice is that all three models do not capture the observed electron loss at low L^* regions, which could be due to other loss mechanisms than magnetopause shadowing, such as the scattering loss induced by the interaction with waves (e.g., EMIC waves), which are beyond the scope of this study. Overall, our results show that Model 3 utilizing the LCDS obtained through tracing test particles and physically including DOB agrees the best with the observations.

4.3.3 Simulation Results in Flux

The model-data comparison presented above is for a fixed set of μ and K values. For a comprehensive comparison with data, we perform the simulation for different μ and K values and then convert the modeled PSD to electron flux in energy and pitch angle space to directly compare with the flux observations. Figure 4.3a presents the observed pitch angle distributions (PAD) of electron fluxes at 2.1 MeV along the orbit of Van Allen Probe A (identical to Figure 4.1c), while

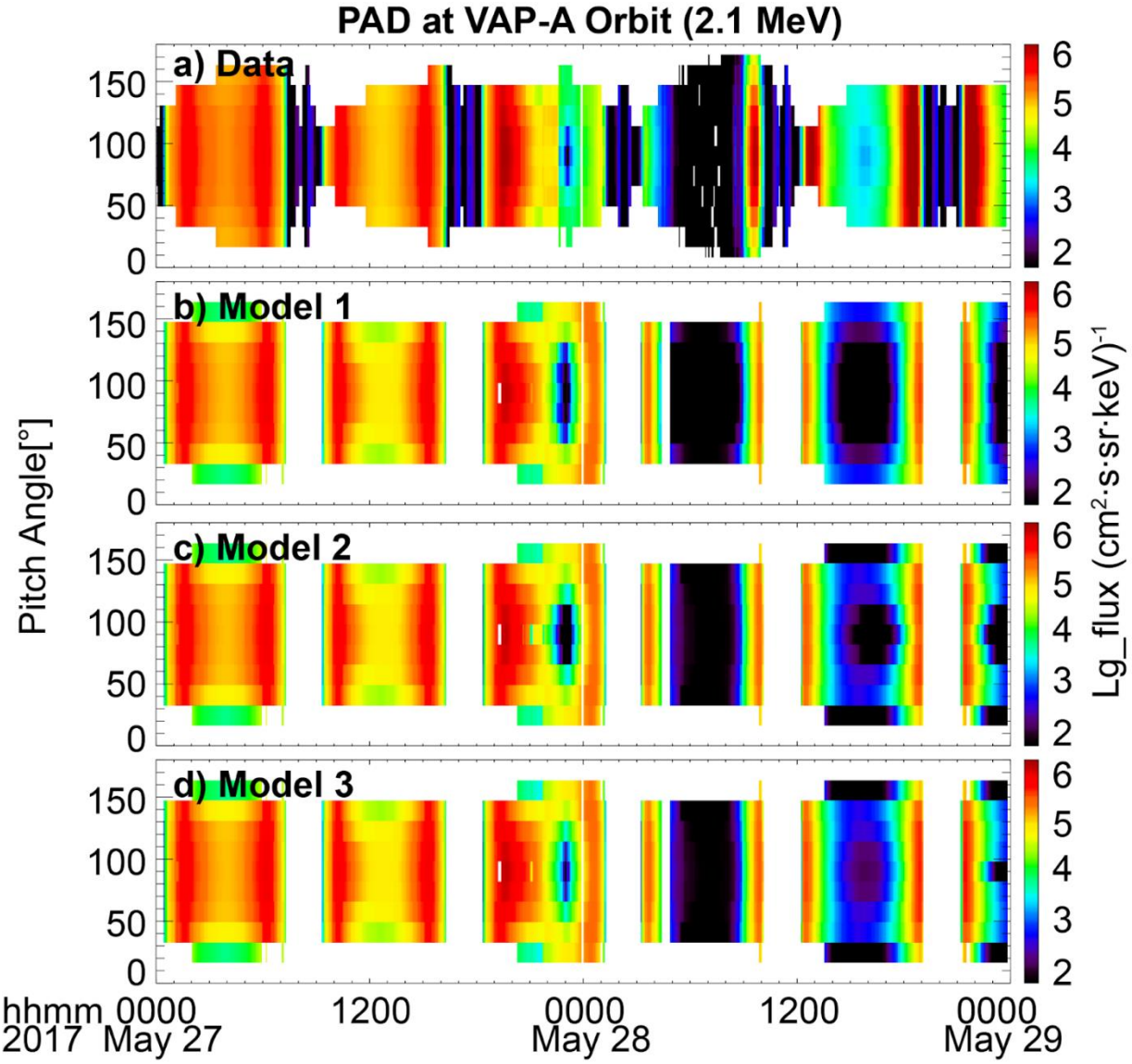

Figure 4.3: Observed (a) and modeled (b-d) pitch angle distributions of electron fluxes at 2.1 MeV along Van Allen Probe A's orbit. The models 1-3 in panels (b-d) correspond to the different model settings depicted in Figure 4.2 panels (a3-a5).

Figure 4.3b to 4.3d display the modeled PAD of electron fluxes along the orbit of Probe A. The comparison shows that all models successfully reproduce the observed flux dropout between 5-9UT of May 28 as well as the butterfly distribution near the apogee of Probe A around 23UT of May 27, confirming the dominant effect of magnetopause shadowing loss in this dropout event at high L^*. Nevertheless, for the modeled butterfly PAD, Model 1 overestimates the electron loss for pitch angles ranging from approximately 50° to 130° (comparing Figure 4.3b to 4.3a). Model 2 also overestimates the electron loss at high pitch angles between approximately 65° and 115° (Figure 4.3c), and the overestimation is more pronounced compared to Model 1, while Model 3 exhibits the best agreement with the data. Therefore, the PAD comparison in flux also demonstrates that modeling the magnetopause shadowing loss with the LCDS obtained by tracing particles and physically including DOB could better capture the electron loss at high L^* and outperforms the other two approaches employing LCDS either by tracing field lines or tracing test particles with rejecting DOB, both of which overestimate the observed losses.

4.4 Conclusions and Discussion

During the May 2017 geomagnetic storm event, the electron PSD data calculated based on Van Allen Probes flux measurements show fast loss at large L^* across a wide range of μ values, as well as a butterfly pitch angle distribution in electron fluxes. These features highlight the significant role of magnetopause shadowing loss in the observed electron dropout. In this study, for the first time, we introduce an event-specific and K-dependent LCDS that physically includes the DOB effects, in comparison with two other LCDS that are less physical in addressing DOB, into a 1D radial diffusion model to quantitatively model the effects of DOB in the magnetopause shadowing loss of outer radiation belt electrons. Our major findings can be summarized as follows:

1. The fast dropout of outer radiation belt electrons at high L^* are dominated by magnetopause shadowing loss during this event. The shadowing loss is effectively reproduced by our radial diffusion model utilizing event-specific and K-dependent LCDS, suggesting that the inclusion of event-specific and K-dependent LCDS is crucial for accurately replicating the detailed features of the magnetopause shadowing loss, including its timing, location, and the butterfly pitch angle distribution of electrons.

2. During most of the storm, due to the significant DOB effects, the LCDS calculated by tracing test particles and rejecting DOB is smaller than the LCDS obtained by tracing field lines with constant second adiabatic invariant (ignoring DOB), and both are smaller than the LCDS obtained by tracing particles and physically including DOB. The differences among the calculated LCDS using the three approaches could vary depending on the geomagnetic conditions. For example, during part of the main phase of the studied storm event, when the bifurcation region is narrower, the difference between the LCDS calculated from tracing test particles by rejecting vs. including DOB become smaller.

3. By implementing the LCDS using the three different approaches into our radial diffusion model, we find that using the LCDS from tracing field lines overestimates the electron dropout during both the initial storm phase and main phase at high L^*, while using the LCDS from tracing test particles with rejecting DOB overestimates the loss during the initial storm phase. However, using the LCDS from tracing test particles while physically including DOB reduces the overestimation of shadowing loss during both storm initial and main phases and agrees the best with observations, in both the PSD vs. L^* profiles and the flux pitch angle distributions.

Our results demonstrate the important role of DOB effects on the magnetopause shadowing loss of radiation belt electrons. For the future, there is still more work to be performed to further improve the LCDS calculation and physically include the DOB effects. Firstly, another loss mechanism of energetic electrons at large *L* regions, i.e., field line curvature scattering (FLCS) (Tu et al., 2014a), could scatter electrons into the loss cone and affect the LCDS of electrons. However, FLCS cannot be included in the guiding center test particle simulations since the first adiabatic invariant is violated. To approximately account for the FLCS effects, in this study we examine the change in the second invariant *K* at nightside, and the electrons are assumed to be lost if the change exceeds 0.2. Secondly, our results show that the DOB effects are dependent on the geomagnetic field conditions, thus their effects on magnetopause shadowing loss could vary among different storms. Future investigations examining various storms are necessary to better understand the effects of DOB on electron shadowing loss. Furthermore, it would be worthwhile to explore different magnetic models in the LCDS calculation such as the TS07 model (Tsyganenko & Sitnov, 2007) since the LCDS values can differ significantly among different field models (Albert et al., 2018). Finally, in this work we only explore the DOB effects on the LCDS of electrons using a 1D radial diffusion model, to more comprehensively include the electron transport due to DOB in both electron pitch angle and radial distance (e.g., Huang et al., 2022), a 3D diffusion model like DREAM3D diffusion model (Tu et al., 2013) is needed and will be utilized in the future.

Chapter 5

Conclusion

5.1 Summary and Conclusions

The primary goal of this work is to investigate the effects of drift orbit bifurcation (DOB) on the transport and loss of radiation belt electrons, a significant yet under-studied process in the dynamics of radiation belt electrons. By quantifying the DOB effects on electron transport and incorporating these effects into a global model of radiation belt electrons, we can enhance our understanding of the DOB effects and their relative contribution to outer radiation belt dynamics. However, additional efforts are still required to fully unravel them.

The loss and source mechanisms of radiation belt electrons due to wave-particle interactions have been extensively studied. However, the transport mechanism DOB in absence of waves remains a controversial and poorly understood topic. DOB occurs when the dayside magnetosphere is compressed by the solar wind, leading to changes in the environmental magnetic field that are faster than the particle's bounce motion. This results in the violation of the second adiabatic invariant (I), and renders the third adiabatic invariant (L^*) undefined. In contrast, the first adiabatic invariant and the magnetic field strength at the particle's bouncing mirror points (B_m) remain constant. Therefore, the particle experiences transport in both I and radial distance.

To directly quantify the transport of relativistic electrons when DOB occurs, we use a guiding center test particle code in Chapter 3 to model both the short-term and long-term transport of electrons in I and equatorial radial distance at midnight (L_M) using the T89c magnetic field model under various electron and geomagnetic conditions. Both traditional and nontraditional

DOB transport are revealed from the short-term simulation results after one drift. In traditional DOB transport, electrons experience ballistic jumps at large equatorial pitch angles (defined as the ballistic regime), and diffusive transport at small equatorial pitch angles (defined as the diffusive regime). However, in nontraditional DOB, electrons exhibit diffusive transport in the traditional ballistic regime and ballistic jumps in the traditional diffusive regime. The nontraditional DOB is reported by us for the first time, which we find to be caused by three local B minima along the magnetic field line, unlike traditional DOB cases with two local B minima. Although statistically the nontraditional DOB effects are found to have a minor effect on the transport of electrons based on our results, their distinct and unique transport behavior is still of interest. Our findings further suggest that the effects of DOB are more pronounced for electrons with higher initial energies, at larger initial L_M values, and under higher Kp conditions. Our results also demonstrate that DOB can penetrate inside the geosynchronous orbit at $Kp \geqslant 3$, and the jump in L_M due to DOB can be significant for high equatorial pitch angle electrons. From long-term simulation results of DOB transport of electrons over multiple electron drifts, we calculate the diffusion coefficients for electrons in the diffusive regime. The diffusion coefficients in I as D_{II} and in L_M as $D_{L_ML_M}$ are found to be higher at higher electron equatorial pitch angles and energies at larger initial L_M and Kp values. Notably, the DOB-induced drift averaged D_{II} could be two orders of magnitude higher than the bounce-averaged D_{II} due to pitch angle diffusion by chorus waves. Furthermore, the DOB-induced $D_{L_ML_M}$ could be comparable to or even higher than the D_{LL} driven by ULF waves at high electron equatorial pitch angles. These findings suggest that DOB could lead to significant transport of energetic electrons even in the absence of waves, contributing to the fast dropout of radiation belt electrons. Furthermore, the long-term simulation results for electrons in the ballistic regime show that their transport could be approximated as a combination of advection and

diffusion, with the electrons undergoing a ballistic jump in I and L_M after the first drift and then diffusive transport afterward. The long-term transport rates of electrons due to DOB quantified in Chapter 3 are very useful and can be applied to global radiation belt modeling to study the relative importance of DOB to the loss and transport of radiation belt electrons.

In addition to the diffusion rates due to DOB that were quantified in Chapter 3, we improved the last closed drift shell (LCDS) calculations in Chapter 4 for modeling the magnetopause shadowing loss by physically incorporating the effects of DOB. The traditional approach to LCDS calculations, which is not physical, overlooks the contribution of DOB effects. In Chapter 4, we presented three approaches of LCDS calculations. These approaches include the traditional approach of tracing magnetic field lines with constant I and B_m values, which is not physical and overlooks the DOB effects; the approach using the guiding center test particle code while rejecting DOB (assuming that electrons on bifurcated drift shells are lost); the guiding center test particle approach that physically includes DOB (by calculating the magnetic fluxes enclosed by the bifurcated drift shells to obtain pseudo-L*). We find that the LCDS values derived from these approaches for specific events vary significantly. Then by implementing these event-specific LCDS values into our radial diffusion model, we find that the shadowing loss at large L* regions is effectively reproduced by the model. This indicates that the fast dropout of outer radiation belt electrons is predominantly driven by magnetopause shadowing loss due to low LCDS values, and that the inclusion of event-specific and K-dependent LCDS is crucial for accurately replicating the detailed features of the dropout. More importantly, we found that using the LCDS calculation by tracing test particles and physically including DOB best capture the observed loss at high L* by reducing the overestimated magnetopause shadowing loss by the other two approaches. This

demonstrates the importance of DOB effects in modeling the magnetopause shadowing loss of radiation belt electrons.

Individually, these studies highlight the significance of DOB effects on the transport and loss of radiation belt electrons. Collectively, they contribute to a more comprehensive understanding of the DOB effects, which have not received enough attention or been sufficiently studied previously. The DOB effects can lead to effective loss and transport of radiation belt electrons, and in the modeling work of magnetopause shadowing loss, physically including these effects can better reproduce the observed dropout of radiation belt electrons using event-specific LCDS. These findings improve our physical understanding of the source, loss, and transport of radiation belt electrons, contributing to a more holistic view of their dynamics.

5.2 Future Work

Future work building upon this dissertation includes using the 3D diffusion model to incorporate changes in the adiabatic invariants due to DOB, investigating the DOB effects under different geomagnetic conditions using various magnetic field models, and considering other processes such as field line curvature scattering (FLCS) that may affect the DOB effects.

Unlike ULF waves, which resonate with the electrons and only change the third adiabatic invariant, DOB effects violate the second adiabatic invariant and render the third adiabatic invariant undefined. The diffusion rates due to DOB calculated in Chapter 3 need to be implemented in global radiation belt models to simulate the observed dynamics of radiation belt electrons. Specifically, for the radial diffusion coefficient quantified in Chapter 3, it is more physical to quantify the transport in the pseudo-L^* (equivalent to the generalized $\bar{L}$ parameter proposed by Ukhorskiy et al. (2014)) rather than the radial distance at midnight. The calculation

and implementation of this new pseudo-L^* parameter is a subject of our future study. Importantly, the 1D radial diffusion model presented in Chapter 4 is incapable of capturing the coupled change of second and third adiabatic invariants of electrons due to DOB. Therefore, we need to use the 3D diffusion models, like the DREAM3D diffusion model, to capture the changes in the adiabatic invariants by DOB for a more physical and comprehensive implementation of the DOB effects.

On the other hand, the DOB effects highly depend on the geomagnetic conditions, meaning the accuracy of the magnetic field models is crucial to modeling the DOB effects. The T89c magnetic field model is used in Chapter 3 due to its sole determinant parameter *Kp*. This simplifies the implementation of the diffusion rates due to DOB and makes it easier to compare with diffusion rates from other sources in the literature. However, as seen in the differences between the locations of the three local *B* minima in the T89c and TS04 magnetic models, DOB effects might vary in more realistic magnetic models and under different geomagnetic storm conditions. The work in Chapter 4, which was based solely on one event using the TS04 model, revealed some abnormal field lines which may not exist in other field models. Therefore, future work should explore different magnetic field models and more geomagnetic storm events to comprehensively investigate the DOB effects.

Finally, other processes like FLCS can occur simultaneously with DOB, violating the first adiabatic invariant and leading to additional pitch angle transport of electrons. The effects of FLCS are not considered in the studies of Chapter 3 and Chapter 4. However, it is also important to investigate their relative significance on electron transport. In the future, it would be beneficial to identify regions dominated by these additional processes and incorporate the resulting electron transport into global radiation belt models together with the DOB effects.

Bibliography

Abel, B., Thorne, R. M., & Vampola, A. L. (1994). Solar cyclic behavior of trapped energetic electrons in Earth's inner radiation belt. *Journal of Geophysical Research*, *99*, 427–431. https://doi.org/10.1029/94ja01626

Albert, J. M. (2014). Radial diffusion simulations of the 20 September 2007 radiation belt dropout. *Annales de Geophysique*, *32*(8), 925-934. https://doi.org/10.5194/angeo-32-925-2014

Albert, J. M., Selesnick, R. S., Morley, S. K., Henderson, M. G., & Kellerman, A. C. (2018). Calculation of last closed drift shells for the 2013 GEM radiation belt challenge events. *Journal of Geophysical Research: Space Physics*, *123*(11), 9597–9611. https://doi.org/10.1029/2018JA025991

Alekseev, I. I., & Shabansky, V. P. (1972). A model of a magnetic field in the geomagnetosphere. *Planetary and Space Science*, *20*(1), 117–133. https://doi.org/10.1016/0032-0633(72)90146-8

Ali, A. F., Malaspina, D. M., Elkington, S. R., Jaynes, A. N., Chan, A. A., Wygant, J., & Kletzing, C. A. (2016). Electric and magnetic radial diffusion coefficients using the Van Allen probes data. *Journal of Geophysical Research: Space Physics*, *121*(10), 9586–9607. https://doi.org/10.1002/2016JA023002

Allen, J. (2010). The galaxy 15 anomaly: Another satellite in the wrong place at a critical time. *Space Weather*, *8*(6), S06008. https://doi.org/10.1029/2010SW000588

Baker, D. N. (2001). Satellite anomalies due to space storms. In *Space storms and space weather hazards* (pp. 285-311). Springer. https://doi.org/10.1007/978-94-010-0983-6_11

Baker, D. N., & Kanekal, S. (2008). Solar cycle changes, geomagnetic variations, and energetic particle properties in the inner magnetosphere. *Journal of Atmospheric and Solar-Terrestrial Physics*, *70*(2-4), 195-206. https://doi.org/10.1016/j.jastp.2007.08.031

Baker, D.N., Erickson, P.J., Fennell, J.F. et al. (2018). Space Weather Effects in the Earth's Radiation Belts. *Space Science Reviews*, *214*(17). https://doi.org/10.1007/s11214-017-0452-7

Baker, D. N., Kanekal, S. G., Hoxie, V. C., Batiste, S., Bolton, M., Li, X., et al. (2013). The Relativistic Electron-Proton Telescope (REPT) instrument on board the Radiation Belt Storm Probes (RBSP) spacecraft: Characterization of Earth's radiation belt high-energy particle populations. *Space Science Reviews*, *179*(1–4), 337–381. https://doi.org/10.1007/s11214-012-9950-9

Baker, D. N., Pulkkinen, T. I., Li, X., Kanekal, S. G., Ogilvie, K. W., Lepping, R. P., et al. (1998a). A strong CME-related magnetic cloud interaction with the Earth's magnetosphere: ISTP observations of rapid relativistic electron acceleration on May 15, 1997. *Geophysical Research Letters*, *25*(15), 2975–2978. https://doi.org/10.1029/98GL01134

Baker, D. N., Pulkinnen, T., Li, X., Kanekal, S. G., Blake, J. B., Selesnick, R. S., et al. (1998b). Coronal mass ejections, magnetic clouds, and relativistic magnetospheric electron events. Journal of Geophysical Research, 103, 17279–17291. https://doi.org/10.1029/97JA03329

Barker, A. B., Li, X., & Selesnick, R. S. (2005). Modeling the radiation belt electrons with radial diffusion driven by the solar wind. *Space Weather*, *3*(10). https://doi.org/10.1029/2004SW000118

Baumjohann, W., & Treumann, R. A. (1996). Basic Space Plasma Physics. World Scientific Book. https://doi.org/10.1142/p015

Blake, J. B., Carranza, P. A., Claudepierre, S. G., Clemmons, J. H., Crain, W. R., Dotan, Y., et al. (2013). The Magnetic Electron Ion Spectrometer (MagEIS) instruments aboard the Radiation Belt Storm Probes (RBSP) spacecraft. *Space Science Reviews*, *179*(1–4), 383–421. https://doi.org/10.1007/s11214-013-9991-8

Blake, J. B., Kolasinski, W. A., Fillius, R. W., & Mullen, E. G. (1992). Injection of electrons and protons with energies of tens of MeV into $L < 3$ on 24 March 1991. *Geophysical Research Letters*, *19*(8), 821–824. https://doi.org/10.1029/92GL00624

Blum, L. W., Halford, A., Millan, R., Bonnell, J. W., Goldstein, J., Usanova, M., et al. (2015). Observations of coincident EMIC wave activity and duskside energetic electron precipitation on 18–19 January 2013. *Geophysical Research Letters*, *42*(14), 5727–5735. https://doi.org/10.1002/2015GL065245

Blum, L. W., Schiller, Q., Li, X., Millan, R., Halford, A., & Woodger, L. (2013). New conjunctive cubesat and balloon measurements to quantify rapid energetic electron precipitation. *Geophysical Research Letters*, *40*(22), 5833–5837. https://doi.org/10.1002/2013GL058546

Borovsky, J. E., Delzanno, G. L., Valdivia, J. A., Moya, P. S., Stepanova, M., Birn, J., Blum, L. W., Lotko, W., & Hesse, M. (2020). Outstanding questions in magnetospheric plasma physics: The pollenzo view. *Journal of Atmospheric and Solar-Terrestrial Physics*, *208*, 1364-6826. https://doi.org/10.1016/j.jastp.2020.105377

Brautigam, D. H., & Albert, J. M. (2000). Radial diffusion analysis of outer radiation belt electrons during the October 9, 1990, magnetic storm, *Journal of Geophysical Research, Space Physics*, *105*(A1), 291-309. https://doi.org/10.1029/1999ja900344

Brizard, A. J., & Chan, A. A. (1999). Nonlinear relativistic gyrokinetic Vlasov-Maxwell equations, *Physics of Plasmas*, *6*(12), 4548-4558. https://doi.org/10.1063/1.873742

Cary, J. R., Escande, D. F., & Tennyson, J. L. (1986). Adiabatic-invariant change due to separatrix crossing, *Physical Review Letters*, *34*(5), 4256-4275. https://doi.org/10.1103/PhysRevA.34.4256

Capannolo, L., Li, W., Ma, Q., Shen, X.-C., Zhang, X.-J., Redmon, R. J., et al. (2019). Energetic electron precipitation: Multievent analysis of its spatial extent during EMIC wave activity. *Journal of Geophysical Research: Space Physics*, *124*(4), 2466–2483. https://doi.org/10.1029/2018JA026291

Chen, Y., Reeves, G. & Friedel, R. (2007). The energization of relativistic electrons in the outer Van Allen radiation belt. *Nature Physics*, 3, 614–617. https://doi.org/10.1038/nphys655

Desai, R. T., Eastwood, J. P., Horne, R. B., Allison, H. J., Allanson, O., Watt, C. E. J., et al. (2021). Drift orbit bifurcations and cross-field transport in the outer radiation belt: Global MHD and integrated test-particle simulations. *Journal of Geophysical Research: Space Physics*, *126*(10), e2021JA029802. https://doi.org/10.1029/2021JA029802

Elkington, S. R., Hudson, M. K., & Chan, A. A. (1999). Acceleration of relativistic electrons via drift-resonant interaction with toroidal-mode Pc-5 ULF oscillations. *Geophysical Research Letters*, *26*(21), 3273–3276. https://doi.org/10.1029/1999GL003659

Fälthammar, C.-G. (1965). Effects of time-dependent electric fields on geomagnetically trapped radiation, *Journal of Geophysical Research*, *70*(11), 2503–2516. https://doi.org/10.1029/JZ070i011p02503

George, H., Reeves, G., Cunningham, G., Kalliokoski, M. M. H., Kilpua, E., Osmane, A., et al. (2022). Contributions to loss across the magnetopause during an electron dropout event. *Journal of Geophysical Research: Space Physics*, *127*(10), e2022JA030751. https://doi.org/10.1029/2022JA030751

Gonzalez, W. D., Joselyn, J. A., Kamide, Y., Kroehl, H. W., Rostoker, G., Tsurutani, B. T., & Vasyliunas, V. M. (1994). What is a geomagnetic storm? *Journal of Geophysical Research*, *99*(A4), 5771–5792. https://doi.org/10.1029/93ja02867

Henderson, M., Morley, S., Niehof, J., & Larsen, B. (2018). drsteve/LANLGeoMag v1.5.16. https://doi.org/10.5281/zenodo.1195041

Horne, R. B., & Thorne, R. M. (1998). Potential waves for relativistic electron scattering and stochastic acceleration during magnetic storms. *Geophysical Research Letters*, *25*(15), 3011–3014. https://doi.org/10.1029/98GL01002

Horne, R. B., Thorne, R. M., Glauert, S. A., Albert, J. M., Meredith, N. P., & Anderson, R. R. (2005). Timescale for radiation belt electron acceleration by whistler mode chorus waves. *Journal of Geophysical Research*, *110*(A3), 3225. https://doi.org/10.1029/2004JA010811

Horne, R. B., Thorne, R. M., Glauert, S. A., Meredith, N. P., Pokhotelov, D., & Santolik, O. (2007). Electron acceleration in the Van Allen radiation belts by fast magnetosonic waves. *Geophysical Research Letters*, *34*(17), L17107. https://doi.org/10.1029/2007GL030267

Huang, J., Tu, W., & Eshetu, W. W. (2022). Modeling the effects of drift orbit bifurcation on radiation belt electrons. *Journal of Geophysical Research: Space Physics*, *127*(11), e2022JA030827. https://doi.org/10.1029/2022JA030827

Hudson, M. K., Elkington, S. R., Lyon, J. G., & Goodrich, C. C. (2000). Increase in relativistic electron flux in the inner magnetosphere: ULF wave mode structure. *Advances in Space Research*, *25*, 2327–2337. https://doi.org/10.1016/S0273-1177(99)00518-9

Jaynes, A. N., Baker, D. N., Singer, H. J., Rodriguez, J. V., Loto'aniu, T. M., Ali, A. F., et al. (2015). Source and seed populations for relativistic electrons: Their roles in radiation belt changes. *Journal of Geophysical Research: Space Physics*, *120*(9), 7240–7254. https://doi.org/10.1002/2015JA021234

Katsavrias, C., Daglis, I. A., & Li, W. (2019). On the statistics of acceleration and loss of relativistic electrons in the outer radiation belt: A superposed epoch analysis. *Journal of Geophysical Research: Space Physics*, *124*(4), 2755–2768. https://doi.org/10.1029/2019JA026569

Kim, H.-J., & Chan, A. A. (1997). Fully adiabatic changes in storm-time relativistic electron fluxes. *Journal of Geophysical Research*, *102*(A10), 22107–22116. https://doi.org/10.1029/97JA01814

Kim, K.-C., Shprits, Y., Subbotin, D., & Ni, B. (2012). Relativistic radiation belt electron responses to GEM magnetic storms: Comparison of CRRES observations with 3-D VERB simulations. *Journal of Geophysical Research*, *117*(A8), A08221. https://doi.org/10.1029/2011JA017460

Koskinen, H. E. J., & Kilpua, E. K. J. (2022). *Physics of Earth's radiation belts*. Springer International Publishing. https://doi.org/10.1007/978-3-030-82167-8

Li, X., Temerin, M., Baker, D. N., Reeves, G. D., & Larson, D. (2001). Quantitative prediction of radiation belt electron at geostationary orbit based on solar wind measurements. *Geophysical Research Letters*, *28*(9), 1887–1890. https://doi.org/10.1029/2000GL012681

Lorentzen, K. R., Blake, J. B., Inan, U. S., & Bortnik, J. (2001). Observations of relativistic electron microbursts in association with VLF chorus. *Journal of Geophysical Research*, *106*(A4), 6017–6027. https://doi.org/10.1029/2000JA003018

Lyons, L. R., & Thorne, R. M. (1973). Equilibrium structure of radiation belt electrons. *Journal of Geophysical Research*, *78*(13), 2142–2149. https://doi.org/10.1029/JA078i013p02142

Lyons, L. R., Thorne, R. M., & Kennel, C. F. (1972). Pitch-angle diffusion of radiation belt electrons within the plasmasphere. *Journal of Geophysical Research*, *77*(19), 3455–3474. https://doi.org/10.1029/JA077i019p03455

Lyu, X., Ma, Q., Tu, W., Li, W., & Capannolo, L. (2022). Modeling the simultaneous dropout of energetic electrons and protons by EMIC wave scattering. *Geophysical Research Letters*, *49*(20), e2022GL101041. https://doi.org/10.1029/2022GL101041

Mauk, B. H., Cohen, I. J., Westlake, J. H., & Anderson, B. J. (2016). Modeling magnetospheric energetic particle escape across Earth's magnetopause as observed by the MMS mission. *Geophysical Research Letters*, *43*(9), 4081–4088. https://doi.org/10.1002/2016GL068856

McIlwain, C. E. (1961). Coordinates for mapping the distribution of magnetically trapped particles. *Journal of Geophysical Research*, *66*(11), 3681–3691. https://doi.org/10.1029/JZ066i011p03681

Meredith, N. P., Horne, R. B., Glauert, S. A., & Anderson, R. R. (2007). Slot region electron loss timescales due to plasmaspheric hiss and lightning generated whistlers. *Journal of Geophysical Research*, *112*(A8), A08214. https://doi.org/10.1029/2006JA012413

Meredith, N. P., Horne, R. B., Glauert, S. A., Thorne, R. M., Summers, D., Albert, J. M., & Anderson, R. R. (2006). Energetic outer zone electron loss timescales during low geomagnetic activity. *Journal of Geophysical Research*, *111*(A5), A05212. https://doi.org/10.1029/2005JA011516

Meredith, N. P., Thorne, R. M., Horne, R. B., Summers, D., Fraser, B. J., & Anderson, R. R. (2003). Statistical analysis of relativistic electron energies for cyclotron resonance with EMIC waves observed on CRRES. *Journal of Geophysical Research*, *108*(A6), 1250. https://doi.org/10.1029/2002JA009700

Nakamura, R., Blake, J. B., Elkington, S. R., Baker, D. N., Baumjohann, W., & Klecker, B. (2002). Relationships between ULF waves and radiation belt electrons during the March 10, 1998 storm. *Advances in Space Research*, *30*(10), 2163. https://doi.org/10.1016/S0273-1177(02)80210-1

O'Brien, T. P., Looper, M. D., & Blake, J. B. (2004). Quantification of relativistic electron microburst losses during the GEM storms. *Geophysical Research Letters*, *31*(4), L04802. https://doi.org/10.1029/2003GL018621

Olifer, L., Mann, I. R., Morley, S. K., Ozeke, L. G., & Choi, D. (2018). On the role of last closed drift shell dynamics in driving fast losses and Van Allen radiation belt extinction. *Journal of Geophysical Research: Space Physics*, *123*(5), 3692–3703. https://doi.org/10.1029/2018JA025190

Olifer, L., Mann, I. R., Ozeke, L. G., Claudepierre, S. G., Baker, D. N., & Spence, H. E. (2021). On the similarity and repeatability of fast radiation belt loss: Role of the last closed drift shell. *Journal of Geophysical Research: Space Physics*, *126*(11), e2021JA029957. https://doi.org/10.1029/2021JA029957

Ozeke, L. G., Mann, I. R., Murphy, K. R., Jonathan Rae, I., & Milling, D. K. (2014). Analytic expressions for ULF wave radiation belt radial diffusion coefficients. *Journal of Geophysical Research: Space Physics*, *119*(3), 1587–1605. https://doi.org/10.1002/2013JA019204

Ozeke, L. G., Mann, I. R., Murphy, K. R., Sibeck, D. G., & Baker, D. N. (2017). Ultra-relativistic radiation belt extinction and ULF wave radial diffusion: Modeling the September 2014 extended dropout event, *Geophysical Research Letters*, *44*(6), 2624-2633. https://doi.org/10.1002/2017GL072811

Öztürk, M. K., & Wolf, R. A. (2007). Bifurcation of drift shells near the dayside magnetopause. *Journal of Geophysical Research*, *112*(A7), A07207.https:// doi.org/10.1029/2006JA012102

Pierrard, V., Botek, E., Ripoll, J.-F., & Cunningham, G. (2020). Electron dropout events and flux enhancements associated with geomagnetic storms observed by PROBA-V/Energetic Particle Telescope from 2013 to 2019. *Journal of Geophysical Research: Space Physics*, *125*(12), e2020JA028487. https://doi.org/10.1029/2020JA028487

Pollock, C., C:son-Brandt, P., Burch, J., et al. (2003). The Role and Contributions of Energetic Neutral Atom (ENA) Imaging in Magnetospheric Substorm Research. *Space Science Reviews*, *109*, 155–182. https://doi.org/10.1023/B:SPAC.0000007518.93331.d5

Potapov, A. S. (2017). Relativistic electrons of the outer radiation belt and methods of their forecast (review). *Solar-Terrestrial Physics*, *1*, 57–72. https://doi.org/10.12737/article_58f9703837c248.84596315

Reeves, G. D., Friedel, R. H. W., Belian, R. D., Meier, M. M., Henderson, M. G., Onsager, T., et al. (1998). The relativistic electron response at geosynchronous orbit during the January 1997 magnetic storm. *Journal of Geophysical Research*, *103*(A8), 17,559–17,570. https://doi.org/10.1029/97JA03236

Reeves, G. D., McAdams, K. L., Friedel, R. H. W., & O'Brien, T. P. (2003). Acceleration and loss of relativistic electrons during geomagnetic storms. *Geophysical Research Letters*, *30*(10), 1529. https://doi.org/10.1029/2002GL016513

Reeves, G. D., Spence, H. E., Henderson, M. G., Morley, S. K., Friedel, R. H. W., Funsten, H. O., et al. (2013). Electron acceleration in the heart of the Van Allen radiation belts. *Science*, *341*(6149), 991–994. https://doi.org/10.1126/science.1237743

Roederer, J. G. (1967). On the adiabatic motion of energetic particles in a model magnetosphere. *Journal of Geophysical Research* (*1896-1977*), *72*(3), 981–992. https://doi.org/10.1029/JZ072i003p00981

Roederer, J. G. (1969). Quantitative models of the magnetosphere. *Reviews of Geophysics*, *7*(1, 2), 77–96. https://doi.org/10.1029/RG007i001p00077

Roederer, J. G. (1970). Dynamics of geomagnetically trapped radiation. In J. G. Roederer & J. Zahringer (Eds.), *Physics and chemistry in space* (Vol. 2, pp. 106-111), Springer. https://doi.org/10.1007/978-3-642-49300-3

Roederer, J. G., & Zhang, H. (2014). *Dynamics of magnetically trapped particles: foundations of the physics of radiation belts and space plasmas.* Astrophysics and space science library, Springer. https://doi.org/10.1007/978-3-642-41530-2

Schulz, M., & Lanzerotti, L. (1974). *Particle diffusion in the radiation belts*. Springer.

Shabansky, V. P. (1972). Phenomenon in the near-Earth space (p. 3) (in Russian).

Shabansky, V. P., & Antonova, A. E. (1968). Topology of particle drift shells in the Earth's magnetosphere (English translation). *Geomagnetism and Aeronomy*, *31*(3), 536–539.

Shprits, Y. Y., Daae, M., & Ni, B. (2012). Statistical analysis of phase space density buildups and dropouts. *Journal of Geophysical Research*, *117*(A1), A01219. https://doi.org/10.1029/2011JA016939

Shprits, Y. Y., Drozdov, A. Y., Spasojevic, M., Kellerman, A. C., Usanova, M. E., Engebretson, M. J., et al. (2016). Wave‐induced loss of ultra-relativistic electrons in the Van Allen radiation belts. *Nature Communications*, *7*(1), 12883. https://doi.org/10.1038/ncomms12883

Shprits, Y. Y., Meredith, N. P., & Thorne, R. M. (2007). Parameterization of radiation belt electron loss timescales due to interactions with chorus waves. *Geophysical Research Letters*, *34*(11), L11110. https://doi.org/10.1029/2006GL029050

Shprits, Y. Y., Thorne, R. M., Friedel, R., Reeves, G. D., Fennell, J., Baker, D. N., & Kanekal, S. G. (2006). Outward radial diffusion driven by losses at magnetopause. *Journal of Geophysical Research*, *111*(A11), A11214. https://doi.org/10.1029/2006JA011657

Summers, D., & Thorne, R. M. (2003). Relativistic electron pitch-angle scattering by electromagnetic ion cyclotron waves during geomagnetic storms. *Journal of Geophysical Research*, *108*(A4), 1143. https://doi.org/10.1029/2002JA009489

Thorne, R. M. (2010). Radiation belt dynamics: The importance of wave-particle interactions. *Geophysical Research Letters*, *37*(22), L22107. https://doi.org/10.1029/2010GL044990

Thorne, R. M., Li, W., Ni, B., Ma, Q., Bortnik, J., Chen, L., et al. (2013). Rapid local acceleration of relativistic radiation-belt electrons by magnetospheric chorus. *Nature*, *504*(7480), 411–414. https://doi.org/10.1038/nature12889

Thorne, R. M., O'Brien, T. P., Shprits, Y. Y., Summers, D., & Horne, R. B. (2005). Timescale for MeV electron microburst loss during geomagnetic storms. *Journal of Geophysical Research*, *110*(A9), 9202. https://doi.org/10.1029/2004JA010882

Tsyganenko, N. A. (1989). A magnetospheric magnetic field model with a warped tail current sheet. *Planetary and Space Science*, *37*(1), 5–20. https://doi.org/10.1016/0032-0633(89)90066-4

Tsyganenko, N. A. (2013). Data-based modelling of the Earth's dynamic magnetosphere: A review. *Annales Geophysicae*, *31*(10), 1745–1772. https://doi.org/10.5194/angeo-31-1745-2013

Tsyganenko, N. A., Andreeva, V. A., & Sitnov, M. I. (2021). Reconstruction of magnetospheric storm-time dynamics using cylindrical basis functions and multi-mission data mining. *Journal of Geophysical Research: Space Physics*, *126*, e2020JA028390. https://doi.org/10.1029/2020JA028390

Tsyganenko, N. A., & Sitnov, M. I. (2005). Modeling the dynamics of the inner magnetosphere during strong geomagnetic storms. *Journal of Geophysical Research*, *110*(A3), A03208. https://doi.org/10.1029/2004JA010798

Tsyganenko, N. A., & Sitnov, M. I. (2007). Magnetospheric configurations from a high-resolution data-based magnetic field model. *Journal of Geophysical Research*, *112*(A6), A06225. https://doi.org/10.1029/2007JA012260

Tu, W., Cowee, M. M., & Liu, K. (2014a). Modeling the loss of inner belt protons by magnetic field line curvature scattering. *Journal of Geophysical Research: Space Physics*, 119(7), 5638–5650. https://doi.org/10.1002/2014JA019864

Tu, W., Cunningham, G. S., Chen, Y., Henderson, M. G., Camporeale, E., & Reeves, G. D. (2013). Modeling radiation belt electron dynamics during GEM challenge intervals with the DREAM3D diffusion model. *Journal of Geophysical Research: Space Physics*, *118*(10), 6197–6211. https://doi.org/10.1002/jgra.50560

Tu, W., Cunningham, G. S., Chen, Y., Morley, S. K., Reeves, G. D., Blake, J. B., et al. (2014b). Event-specific chorus wave and electron seed population models in DREAM3D using the Van

Allen Probes. *Geophysical Research Letters*, *41*(5), 1359–1366. https://doi.org/10.1002/2013GL058819

Tu, W., Li, X., Chen, Y., Reeves, G. D., & Temerin, M. (2009). Storm-dependent radiation belt electron dynamics. *Journal of Geophysical Research*, *114*(A2), A02217. https://doi.org/10.1029/2008JA013480

Tu, W., Selesnick, R., Li, X., & Looper, M. (2010). Quantification of the precipitation loss of radiation belt electrons observed by SAMPEX. *Journal of Geophysical Research, 115*(A7), A07210. https://doi.org/10.1029/2009JA014949

Tu, W., Xiang, Z., & Morley, S. K. (2019). Modeling the magnetopause shadowing loss during the June 2015 dropout event. *Geophysical Research Letters*, *46*(16), 9388–9396. https://doi.org/10.1029/2019GL084419

Turner, D. L., Angelopoulos, V., Morley, S. K., Henderson, M. G., Reeves, G. D., Li, W., et al. (2014). On the cause and extent of outer radiation belt losses during the 30 September 2012 dropout event. *Journal of Geophysical Research: Space Physics*, *119*(3), 1530–1540. https://doi.org/10.1002/2013JA019446

Turner, D. L., Shprits, Y., Hartinger, M., & Angelopoulos, V. (2012). Explaining sudden losses of outer radiation belt electrons during geomagnetic storms. *Nature Physics*, *8*(3), 208–212. https://doi.org/10.1038/nphys2185

Ukhorskiy, A. Y., Anderson, B. J., Brandt, P. C., & Tsyganenko, N. A. (2006). Storm time evolution of the outer radiation belt: Transport and losses. *Journal of Geophysical Research*, *111*(A11), A11S03. https://doi.org/10.1029/2006JA011690

Ukhorskiy, A. Y., Sitnov, M. I., Millan, R. M., & Kress, B. T. (2011). The role of drift orbit bifurcations in energization and loss of electrons in the outer radiation belt. *Journal of Geophysical Research*, *116*(A9), A09208. https://doi.org/10.1029/2011JA016623

Ukhorskiy, A. Y., Sitnov, M. I., Millan, R. M., Kress, B. T., Fennell, J. F., Claudepierre, S. G., & Barnes, R. J. (2015). Global storm time depletion of the outer electron belt. *Journal of Geophysical Research: Space Physics*, *120*(4), 2543–2556. https://doi.org/10.1002/2014ja020645

Ukhorskiy, A. Y., Sitnov, M. I., Millan, R. M., Kress, B. T., & Smith, D. C. (2014). Enhanced radial transport and energization of radiation belt electrons due to drift orbit bifurcations. *Journal of Geophysical Research: Space Physics*, *119*(1), 163–170. https://doi.org/10.1002/2013JA019315

Usanova, M. E., Drozdov, A., Orlova, K., Mann, I. R., Shprits, Y., Robertson, M. T., et al. (2014). Effect of EMIC waves on relativistic and ultra-relativistic electron populations: Ground-based and Van Allen Probes observations. *Geophysical Research Letters*, *41*(5), 1375–1381. https://doi.org/10.1002/2013GL059024

Van Allen, J.A., Ludwig, G.H., Ray, E.C., & McIlwain, C.E. (1958). Observation of high intensity radiation by satellites 1958 alpha and gamma. *Jet Propulsion*, *28*(9), 588–592. https://doi.org/10.2514/8.7396

Van Allen, J.A., McIlwain, C.E., & Ludwig, G.H. (1959). Satellite observations of electrons artificially injected into the geomagnetic field. *Journal of Geophysical Research: Space Physics*, *64*(8), 877-891. https://doi.org/10.1029/JZ064i008p00877

Walach, M.-T., & Grocott, A. (2019). SuperDARN observations during geomagnetic storms, geomagnetically active times, and enhanced solar wind driving. *Journal of Geophysical Research: Space Physics*, *124*(7), 5828–5847. https://doi.org/10.1029/2019JA026816

Wan, Y., Sazykin, S., Wolf, R. A., & Öztürk, M. K. (2010). Drift shell bifurcation near the dayside magnetopause in realistic magnetospheric magnetic fields. *Journal of Geophysical Research: Space Physics*, *115*(A10), A10205. https://doi.org/10.1029/2010JA015395

Welling, D.T., André, M., Dandouras, I., et al. (2015). The Earth: Plasma Sources, Losses, and Transport Processes. *Space Science Reviews*, *192*, 145–208. https://doi.org/10.1007/s11214-015-0187-2

Xiang, Z., Tu, W., Li, X., Ni, B., Morley, S. K., & Baker, D. N. (2017). Understanding the mechanisms of radiation belt dropouts observed by Van Allen Probes. *Journal of Geophysical Research: Space Physics*, *122*(10), 9858–9879. https://doi.org/10.1002/2017JA024487

Xiang, Z., Tu, W., Ni, B., Henderson, M. G., & Cao, X. (2018). A statistical survey of radiation belt dropouts observed by Van Allen Probes. *Geophysical Research Letters*, *45*(16), 8035–8043. https://doi.org/10.1029/2018GL078907

Yu, Y., Koller, J., & Morley, S. K. (2013). Quantifying the effect of magnetopause shadowing on electron radiation belt dropouts. *Annales Geophysicae*, *31*(11), 1929–1939. https://doi.org/10.5194/angeo-31-1929-2013

Yu, Y., Tian, X., & Jordanova, V. K. (2020). The effects of field line curvature (FLC) scattering on ring current dynamics and isotropic boundary. *Journal of Geophysical Research: Space Physics*, *125*(8), e2020JA027830. https://doi.org/10.1029/2020JA027830

Zhang, X.-J., Li, W., Ma, Q., Thorne, R. M., Angelopoulos, V., Bortnik, J., et al. (2016). Direct evidence for EMIC wave scattering of relativistic electrons in space. *Journal of Geophysical Research: Space Physics*, *121*(7), 6620–6631. https://doi.org/10.1002/2016JA022521

Zhao, H., & Li, X. (2013a). Inward shift of outer radiation belt electrons as a function of Dst index and the influence of the solar wind on electron injections into the slot region. *Journal of Geophysical Research*, *118*(2), 756–764. https://doi.org/10.1029/2012JA018179

Zhao, H., & Li, X. (2013b). Modeling energetic electron penetration into the slot region and inner radiation belt. *Journal of Geophysical Research: Space Physics*, *118*(11), 6936–6945. https://doi.org/10.1002/2013JA019240